



大湾区显微科学与技术研究中心

Bay Area Center for Electron Microscopy

简讯

第14期

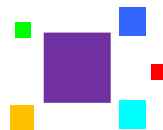
中国科学院东莞材料科学与技术研究所

广东省东莞市大朗镇屏东路333号

Email: bacem@sslabor.org.cn

2025年第3期 (总第14期)

出版日期: 2025年11月1日



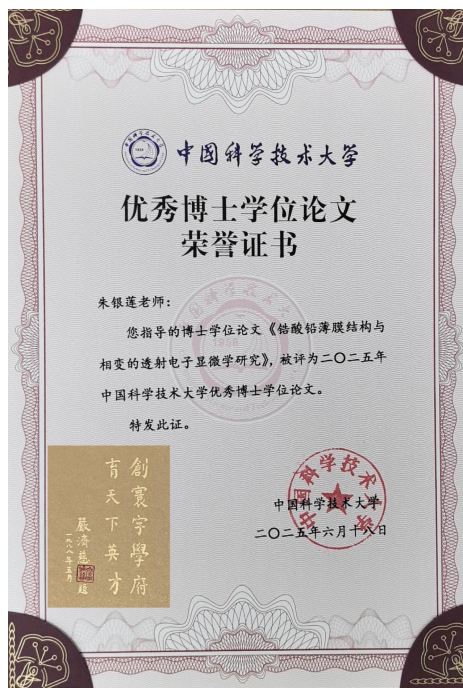
马秀良研究员被授予广东省劳动模范称号

为表彰先进，树立典型，进一步激发全省人民的劳动热情和创造活力，五一劳动节

前夕，省委、省政府决定授予 354 人广东省劳动模范称号，授予 40 人广东省先进工作者称号，授予 97 个集体广东省先进集体称号。其中，大湾区电镜中心马秀良研究员被授予广东省劳动模范称号。马秀良研究员曾于 2023 年获广东省总工会授予的“广东省五一劳动奖章”。

朱银莲研究员指导的学位论文被评为中科大优秀博士学位论文

2025 年 6 月，由大湾区电镜中心朱银莲研究员和金属所唐云龙研究员指导、姜如建同学完成的博士学位论文《锆酸铅薄膜结构与相变的透射电子显微学研究》，被评为 2025 年中国科学技术大学优秀博士学位论文。同时，姜如建也荣获 2025 年度“中国科学院院长奖”优秀奖。该论文在利用精密脉冲激光沉积技术制备高质量反铁电 PbZrO_3 薄膜的基础上，以像差校正电子显微成像为主要研究手段，系统揭示了 PbZrO_3 薄膜中的相组成、相变动力学、尺寸效应以及极化拓扑形态，加深了对反铁电机制及其相关性质的理解，为基于反铁电材料的器件设计与应用提供了重要的基础信息。



耿皖荣副研究员入选“松湖青年学者计划”

“松湖青年学者计划”是松山湖材料实验室为打造高层次人才梯队而设立的青年人才引进与培养计划。其核心目标是面向全球遴选在材料科学及相关交叉领域已有突出学术成就或

展现出巨大潜力的优秀青年学者，通过提供具有国际竞争力的薪酬待遇、充足的科研启动经费和顶尖的科研平台支持，帮助他们独立开展前沿性、挑战性的科学研究，培养他们成为未

来的学术带头人。

经过申报-初审-答辩评审-公示四个阶段，

大湾区显微科学与技术研究中心的耿皖荣副研究员入选 2025 年度“松湖青年学者计划”。

电镜中心三项项目获 2025 国家自然科学基金资助

近日，2025 年国家自然科学基金集中接收申请项目评审结果揭晓。

大湾区显微科学与技术研究中心三项项目获得资助，它们分别是：耿皖荣副研究员的面上基金项目“掺杂 HfO₂ 薄膜界面-氧空位耦合与铁电性调控的亚埃尺度研究”、冯燕朋副研究员的青年基金项目“外场调控铁电极化麦纳拓扑畴的动力学机制研究”、陈雨亭副研究员的青年基金项目“基于原子分辨电子层析成像方法的铁电斯格明子三维原子结构与功能特性解析”。

据悉，2025 年国家自然科学基金项目在集中接收期间，基金委共收到项目申请 433426 项，经初审和复审后共受理 432434 项。根据《国家自然科学基金条例》、国家自然科学基金相关项目管理办法和专家评审意见，经自然科学基金委委务会议审批，资助面上项目、青年科学基金项目（A、B、C 类）、地区科学基金项目、重点项目、创新研究群体项目、重点国际（地区）合作研究项目、外国学者研究基金项目和合作创新研究团队项目等 10 类项目共 53159 项。

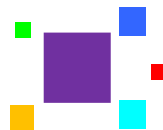
2025 全国电子显微学学术年会在武汉召开

2025 年 9 月 27-29 日，2025 年全国电子显微学学术年会在武汉国际会议中心召开。大会由中国电镜学会电子显微学报编辑部主办，武汉大学、东南大学共同承办。大会为期三天，来自高校院所、企事业单位、仪器技术企业等电子显微学领域专家学者 2000 余人出席参会。

显微学是一个集材料、物理、化学、生命科学等学科深度交叉融合的学科。本届年会按材料科学与生命科学设立十五个专题分会场，包含：01) 显微学理论、仪器方法与技术；02) 原位电子显微学表征；03) 功能材料的微结构表征；04) 结构材料及缺陷、界面、表面，相变与扩散；05) 先进显微分析技术在工业材料中的应用；06) 扫描探针显微学表征；07) 电

子衍射及电子显微全息（含 SEM、EBSD 和 TEM）材料微结构表征；08) 聚焦离子束（FIB）在材料科学中的应用；09) 低温电子显微学表征；10) 生物医学电镜技术发展与应用；11) 显微学在农林及生物科学领域中的应用（超分辨显微镜，激光共聚焦显微镜等）；12) 农林电子显微学研究与应用；13) 先进材料；14) 显微科学仪器与先进材料组织结构表征；15) 大型科研仪器平台建设发展与开放共享。

大湾区显微科学与技术研究中心朱银莲研究员应邀在第四分会作了关于铁电拓扑结构的邀请报告；冯燕朋副研究员获第四分会优秀报告奖；耿皖荣副研究员获第三分会优秀报告奖。冯燕朋、朱银莲、马秀良以及耿皖荣、王宇佳、



朱银莲、马秀良分别获优秀 poster 奖。

耿皖荣副研究员获中国电子显微学会优秀青年学者奖

为促进中国电子显微学事业的发展，尤其为鼓励和支持优秀青年电子显微学人才，中国电子显微学会设立“优秀青年学者奖”。该奖项每年颁发一次，原则上材料科学和生命科学各一人。获奖人应于近年来在电子显微学领域取得具有重要原创性的研究成果并发表在具有重要影响力的学术刊物上，且在获奖当年年龄一般不超过 40 周岁。

经专家推荐和同行评议，大湾区电镜中心耿皖荣副研究员获 2025 中国电子显微学会优

秀青年学者奖。



Steve Pennycook 教授访问大湾区电镜中心

应马秀良研究员的邀请，国际知名电子显微学家、高分辨率 Z 衬度成像技术的开拓者 Steve Pennycook 教授于 2025 年 10 月 10-11 日访问大湾区电镜中心。来访期间，Pennycook 教授与电镜中心科研人员进行了详细的学术交流，并对电镜中心多年来取得的系统性研究成果给予高度评价。

Steve 在 35 岁时首次利用扫描透射电子显微镜下的环型暗场技术获得高分辨率原子序数

(Z) 衬度像 (Nature, 1988)，自此该成像技术成为与传统相干成像技术相平行的一种新的高分辨电子显微技术。目前，与 Z 衬度成像相关的软硬件广泛装备于国际上各类电子显微学实验室，是现代材料电子显微分析不可或缺的重要手段。

Pennycook 教授曾先后任职于英国剑桥大学、美国橡树岭国家实验室、新加坡国立大学等。





铪基薄膜中单斜铁电变体的构筑 (Nature Communications 2025)

近日，大湾区显微科学与技术研究中心团队耿皖荣副研究员等人在铪基薄膜铁电变体的调控研究中取得重要进展。他们在单晶外延 $\text{Hf}_{0.5}\text{Zr}_{0.5}\text{O}_2$ 薄膜中成功稳定具有铁电性的新型单斜相，使材料呈现出卓越的抗铁电疲劳性能，为铪基薄膜中铁电性的稳定与增强开辟了新路径。相关研究成果于 2025 年 10 月 3 日在 Nature Communications 正式发表。

铪基铁电材料凭借其可与 CMOS 工艺高度兼容、在纳米尺度下仍能保持强铁电性等核心优势，被业界广泛视为下一代铁电信息存储材料的核心候选方向。然而，该类材料的应用推广长期面临两大关键瓶颈：一方面， HfO_2 等萤石型铁电材料的铁电性来源于室温环境下的亚稳正交相（空间群 $Pca2_1$ ），而这一亚稳相极易向非极性稳定相转变，导致铁电性能衰减；另一方面，铪基材料在实际制备中常以多相和纳米晶形态存在，其内部高密度的界面与缺陷会进一步加剧正交相的失稳，严重制约了稳定、长寿命铪基铁电器件的研发与应用。

针对上述基础性科学难题，他们以异质结构对称性匹配原则为理论基础，构筑出稳定存

在的新型单斜铁电相。他们通过脉冲激光沉积系统制备出具有单斜结构的 $\text{Hf}_{0.5}\text{Zr}_{0.5}\text{O}_2$ 单晶薄膜。电循环测试结果显示，该薄膜的耐疲劳性能高达 10^{12} 次，远超传统铪基薄膜水平。借助像差校正透射电镜多功能成像技术，明确该薄膜结构为富含反相畴界的非极性单斜相（空间群 $P2_1/c$ ），且证实反相畴界处的对称性失配与晶格应变是诱导极性变体稳定的关键机制。

在此基础上，他们实现了反相畴以单胞尺度连续扩展，进而稳定出新型极性单斜相（空间群 Pc ）。第一性原理计算结果表明，该新型极性相的铁电翻转势垒仅为传统亚稳正交相的 20%–50%，为材料实现低功耗铁电调控提供了结构基础。该项工作不仅为铪基材料中稳定、可控铁电性的实现提供了新思路，更从技术层面为低功耗、长寿命且与硅工艺兼容的铁电器件研发注入了新动力，对推动铁电信息存储、新型电子器件等领域的技术革新具有重要意义。

该研究得到了国家自然科学基金、广东省基础与应用基础研究基金、广东省量子科学战略计划、松山湖科学城显微科学与技术开放课题等多个项目的共同资助和支持。（原文附后）

铁电材料中斯格明子与 180° 畴的遗传关系揭示 (Acta Materialia 2025)

近日，大湾区显微科学与技术研究中心在铁电材料拓扑结构研究领域进一步取得进展，

通过对铁电畴和铁弹畴家族进行分类对比，进一步揭示了斯格明子-泡泡与铁电 180° 畴的遗



传关系,提出了一种新的斯格明子-泡泡的形成机制。相关成果于2025年8月24日发表在 *Acta Materialia* 期刊上。

在2010年,同步辐射实验结果已经检测到了铁电斯格明子-泡泡的信号。遗憾的是当时并未使用透射电子显微镜(TEM)对 $\text{PbTiO}_3/\text{SrTiO}_3$ 超晶格进行研究,这导致人们错误地认为这些畴结构仅仅是 180° 畴,从而使铁电斯格明子-泡泡的发现延迟了十年。这也凸显了 TEM 在材料科学研究中的重要作用。直到2019年,伯克利国家实验室相关人员才在生长于 SrTiO_3 衬底上的 $\text{PbTiO}_3/\text{SrTiO}_3$ 超晶格中观察到了铁电斯格明子-泡泡。在此基础上,我们通过文献调

研,实验和理论相结合的方式,对比分析了 180° 畴和斯格明子-泡泡,认为去极化场重新分割了条状的 180° 畴,导致 180° 畴演化为斯格明子-泡泡,从而推断出斯格明子-泡泡与 180° 畴存在遗传关系,这为斯格明子-泡泡的形成提供了新的认识。

大湾区显微科学与技术研究中心宫风辉、陈雨亭为该论文的共同第一作者,松山湖材料实验室朱银莲研究员和中国科学院金属研究所唐云龙研究员为共同通讯作者。该研究得到了国家自然科学基金、博新计划、博后面上等多个项目的共同资助和支持。(原文附后)

A stable monoclinic variant and resultant robust ferroelectricity in single-crystalline hafnia-based films

Received: 21 September 2024

Accepted: 1 September 2025

Published online: 03 October 2025

Check for updates

Wan-Rong Geng^{1,8}, Yu-Jia Wang^{2,8}, Yin-Lian Zhu^{1,3}, Sirui Zhang⁴, Huiqin Ma⁵, Yun-Long Tang², Shi Tuo⁵ & Xiu-Liang Ma^{1,6,7} ✉

The ferroelectricity in nanoscale HfO₂-based films enables their applications more promising than that of the perovskite oxides, taking into account the easy compatibility with the modern silicon-based semiconductor technology. However, the well-known polar orthorhombic phase is thermodynamically metastable, making the applications of HfO₂-based ferroelectrics challenging in terms of uncontrollability and consequently instability of the physical performance in electronic devices. Here we report the robust ferroelectricity in stable monoclinic Hf_{0.5}Zr_{0.5}O₂ single-crystalline films, which was known as non-polar before. The as-prepared films display high endurance performance of wake-up free and non-fatigue behavior up to 10¹² cycles. Multimode imaging under aberration-corrected scanning transmission electron microscopy reveals that such an unexpected ferroelectric behavior is resultant from an antiphase boundaries-derived monoclinic polar variant (space group, *Pc*) intergrown with the nonpolar monoclinic phase (*P2₁/c*). The switching barrier for the stable polar variant is only 20–50% of that for the metastable orthorhombic phase according to the calculation by the nudged elastic band method. These findings provide a practical approach for designing robust ferroelectricity in hafnia-based materials and would be helpful for the development of lower energy-cost and long-life memory devices compatible with integrated circuit technology.

Ferroelectric materials have a wide range of applications in next-generation switching, logical, and memory devices. However, the widely-studied perovskite-type ferroelectrics are getting limited in practical applications owing to the scaling effects¹ and a low compatibility with the existing Si technology². The emergent ferroelectricity in doped HfO₂ films³ has broken the traditional paradigm and inspired a renewed interest in ferroelectric devices due to the wealth of advantages, including the simple binary structure, robust nanoscale

ferroelectricity⁴, high compatibility with the metal-oxide semiconductor (CMOS) technology^{5,6} and desirable physical properties^{4,5,7–10}.

Nevertheless, HfO₂-based ferroelectric films are usually in the form of polycrystalline and multiphase structures^{11,12}. Despite the prevalent polar orthorhombic phase¹³ and a complementary rhombohedral ferroelectric phase¹⁴ in polycrystalline films, the polymorphic nature of HfO₂ definitely blur the crucial structural origins of the

¹Bay Area Center for Electron Microscopy, Songshan Lake Materials Laboratory, Dongguan, China. ²Shenyang National Laboratory for Materials Science, Institute of Metal Research, Chinese Academy of Sciences, Shenyang, China. ³School of Materials Science and Engineering, Hunan University of Science and Technology, Xiangtan, China. ⁴School of Advanced Materials and Nanotechnology, Xidian University, Xi'an, China. ⁵Zhejiang Laboratory, Hangzhou, China. ⁶Institute of Physics, Chinese Academy of Sciences, Beijing, China. ⁷Quantum Science Center of Guangdong-HongKong-Macau Greater Bay Area (Guangdong), Shenzhen, China. ⁸These authors contributed equally: Wan-Rong Geng, Yu-Jia Wang. ✉ e-mail: xlma@iphy.ac.cn

ferroelectricity and the mechanism of polarization switching. Great efforts have been made to fabricate high-quality, epitaxial, single-crystalline films^{15–18}, stabilize the polar phases^{19,20}, and improve the ferroelectricity^{4,21}, however, these efforts are still challenging at the present stage. These challenges are because of the fact that the orthorhombic phase (space group, $Pca2_1$), which is known to result in the ferroelectricity, is thermodynamically metastable^{4,7,22,23}. So far, various strategies, such as volumetric confinement^{7,9}, dopant concentration^{24,25}, strain²⁶, defect concentration^{21,27}, and surface electrochemical state²⁰, have been adopted to try stabilizing the polar phase in HfO₂-based films. Especially, the constructed nanocrystal grains, whether in ultrathin films or in superlattices, characterized by the high surface-to-volume ratio in these forms, are widely accepted to stabilize the polar orthorhombic phase, based on the fact of its lower surface energy than that of the monoclinic phase^{28,29}. However, the metastable nature of the orthorhombic ferroelectric phase and the inevitable existence of the nonpolar monoclinic phase¹² heavily inhibit the development of HfO₂-based films with facile controllability and endurance performance, thereby hindering the applications at the state-of-the-art technology node³⁰.

Herein, we find robust ferroelectricity in stable monoclinic Hf_{0.5}Zr_{0.5}O₂ (HZO) single-crystalline films, which feature wake-up free and high cycles of non-fatigue property. Such an unexpected ferroelectric behavior is clarified to result from a polar variant intergrown with the nonpolar monoclinic phase. Atomic imaging together with the first-principles calculations indicate that the ferroelectric variant originates a polar state at the antiphase boundaries (APBs), which feature a translation vector of half of the diagonal along [101] direction of the nonpolar monoclinic phase in the HZO films. The constraint of the lattice distortion at the APBs makes the symmetry breaking from the centrosymmetric to the polar variant. More importantly, repeated antiphase boundaries at the unit-cell level in the non-polar monoclinic phase are found to result in the formation of a stable polar phase in the

single-crystalline films with much lower switching barrier (0.102 eV/u.c.), and consequently makes the as-received film display higher endurance behavior compared with that of the metastable orthorhombic phase.

Results

A series of HZO films with the thickness of 10 nm, 15 nm, and 65 nm, respectively, were deposited on a (001)-oriented Y₂O₃:ZrO₂ (YSZ) substrate using the pulsed laser deposition (PLD) method. In these HZO films, the stoichiometric ratio of Hf and Zr is calculated as about 1:1 based on the atomic-resolved EDS elemental maps (Supplementary Fig. 1), which is consistent with the Hf_{0.5}Zr_{0.5}O₂ target used. All the as-grown films are single-crystallized, as seen in the spectrum of a representative XRD θ - 2θ scan of the 65 nm HZO film (Fig. 1a and Supplementary Fig. 2). Only (001) reflection of the monoclinic phase (*m*-HZO) at -17° is identified together with the (001) reflection of the YSZ substrate (Fig. 1a), no reflection of other phases being observed (Supplementary Fig. 2). The clear Laue oscillations near the *m*-HZO (001) diffraction peak suggest a high quality of the crystallization and a smooth interface between the YSZ substrate and the HZO film. The crystallinity of the film is further confirmed according to the XRD rocking curves, which measure the lateral coherence length and the crystallite tilt. As shown in Fig. 1b, the rocking curve is dominated by a sharp peak with the full width at half maximum (FWHM) of 0.013° , indicating the high crystallinity. In the symmetric (001) reciprocal space map (RSM) shown in Fig. 1c, the two reflections of the YSZ substrate and the HZO film have the same in-plane component (Q_x) which indicates that the single crystal HZO film is coherently strained and its in-plane lattice parameter matches with that of the YSZ substrate. The broadening of the *m*-HZO (001) peak might result from the thickness effect, the crystal lattice distortion or even the variation in crystallite domain sizes³¹. The surface topography of the HZO film is further characterized by the atomic force microscopy (AFM), and the

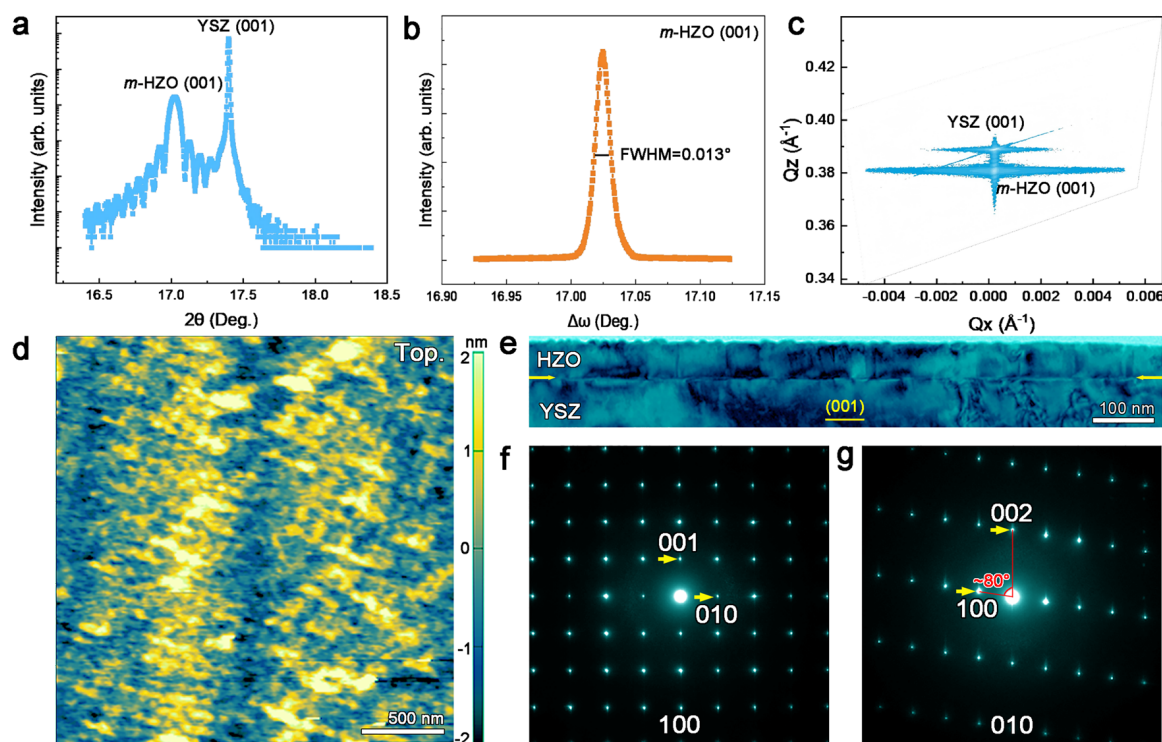


Fig. 1 | Single-crystal of the monoclinic phase in HZO film grown on YSZ (001) substrate. **a** XRD θ - 2θ scan of a 65 nm HZO film with the monoclinic (*m*) structure. **b** Rocking curve of the *m*-HZO (001) peak showing the high crystallinity of the film. **c** RSM analysis, indicating the coherence of the HZO film on the YSZ substrate and

its in-plane lattice parameter of the film matches with that of the substrate. **d** AFM image showing the surface topography of the HZO film with the average roughness of 762 pm. **e** A cross-sectional BF TEM image of the HZO film. **f**, **g** SAED patterns of the HZO film along [100] and [010] zone axis, respectively.

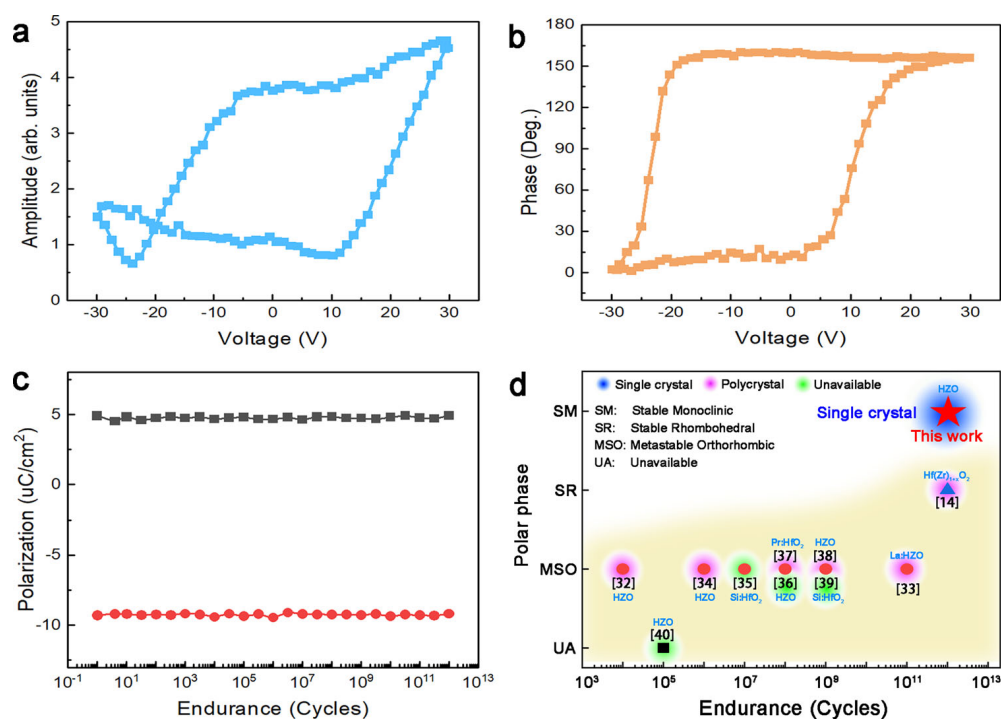


Fig. 2 | Ferroelectric property of the monoclinic HZO single-crystalline film with high endurance. **a, b** Local PFM amplitude and phase hysteresis loops. The intergrowth of the polar variant with the non-polar monoclinic matrix makes the as-grown films displays local ferroelectric switching behavior. **c** Endurance property of

the polar phase, displaying the non-fatigue feature up to 10^{12} field cycles at 10 V and 10 MHz. **d** The endurance performance of the present monoclinic HZO single-crystalline film, comparing to other reported HfO₂-based ferroelectric films with polycrystalline structure^{14,32–40}.

average roughness (Ra) is 762 pm for the region shown in Fig. 1d. The films with thickness of 10 nm and 15 nm are also single-crystallized with the monoclinic structure (Supplementary Fig. 3 and Supplementary Fig. 4, 5). The largest FWHM for the 15 nm HZO film attributes to the defect clusters in this film (Supplementary Fig. 6), which could be induced by the accidental fluctuations in laser power during the film deposition. To directly visualize the epitaxial system in real space, cross-sections of the HZO/YSZ (001) sample with a film thickness of 65 nm are prepared for transmission electron microscopic (TEM) observations. The diffraction contrast in the HZO film is comparable with that of the YSZ substrate, as seen in the bright field (BF) TEM image (Fig. 1e), which indicates that the orientation of the film crystal is basically the same as that of the substrate. The high-quality epitaxial growth is further supported by the elemental mapping, shown in Supplementary Fig. 7, where all the elements are distributed in a homogeneous manner. Selected area electron diffraction (SAED) patterns along [100] and [010] zone axis, respectively, are obtained in the cross-sectional specimens which are prepared in two perpendicular directions. A primitive monoclinic lattice with $\beta \approx 100^\circ$ can be derived according to the SAEDs. In addition, in the [010] electron diffraction pattern (EDP), the $h00$ reflections with $h = \text{odd}$ are extinctions, which indicates the presence of c glide on the (010) plane and therefore a space group of $P2_1/c$ with the lattice parameter of $a = 5.1 \text{ \AA}$, $b = 5.2 \text{ \AA}$, $c = 5.3 \text{ \AA}$, $\beta = 99^\circ$. As a result, the single-crystalline HZO films with the structure being monoclinic phase are epitaxially grown using the PLD method, which is different from the polar orthorhombic HZO films fabricated by atomic layer deposition³².

It is known that the stable monoclinic phase with space group of $P2_1/c$ is nonpolar in HfO₂-based materials. However, it is of great interest to find that the above monoclinic HZO single-crystalline film displays an unexpected robust ferroelectric property. The vertical and lateral PFM images in Supplementary Figs. 8, 9 suggest the robust out-of-plane polarization component and a weak in-plane polarization component. As shown in Fig. 2a, b, the local PFM amplitude and phase

hysteresis loops acquired using piezoresponse force microscopy (PFM) suggest the ferroelectric switching behavior. The local amplitude hysteresis loop in Fig. 2a shows a characteristic butterfly loop. Also, the 180° phase change is reflected in the local phase hysteresis loop under external electric field (Fig. 2b). Besides, the HZO film displays the high endurance performance of wake-up free and shows non-fatigue up to 10^{12} cycles at the test condition of 10 V and 10 MHz (Fig. 2c) using in-plane interdigitated Ti/Au (10 nm/100 nm) electrodes (Supplementary Fig. 10), which is much more remarkable (Fig. 2d) compared with those reported in the literature^{14,33–41}. The asymmetric endurance property in Fig. 2c is expected to be due to the non-uniform electric field and strain distribution at the inter-digitized electrodes and the structural clamping in the HZO films. The ferroelectricity of the HZO film is further qualitatively confirmed by the polarization-electric field curves, endurance tests at varying electric voltages and varying frequencies (Supplementary Figs. 11–16) and the polarization current responses (Supplementary Fig. 17), despite the faint polarization switching current signals. It is noted that the constant polarization values in endurance tests at varying frequencies (Supplementary Figs. 14–16) attribute to the fixed reading frequency of 5 kHz. Despite this, it is seen that the present HZO film with the stable polar monoclinic phase displays the highest endurance behavior in the form of single-crystalline film fabricated by PLD method, compared with the prevalent polycrystal HfO₂-based films.

To illuminate the structure origin of the macroscopical ferroelectricity, extensive investigation on the detailed microstructures in the HZO films is further performed, benefiting from the single crystal epitaxially grown on a YSZ substrate. In addition to the cross-sectional TEM observation as that in Fig. 1e–g, planar-view imaging is also performed, as exemplified in the dark-field TEM image and low-magnification HAADF-STEM image in Fig. 3a. It is of interest to find that the HZO film features high-density domain boundaries with the line-shaped contrasts approximately perpendicular to the [010] and [100] directions. The growth of the HZO film is likely in the columnar

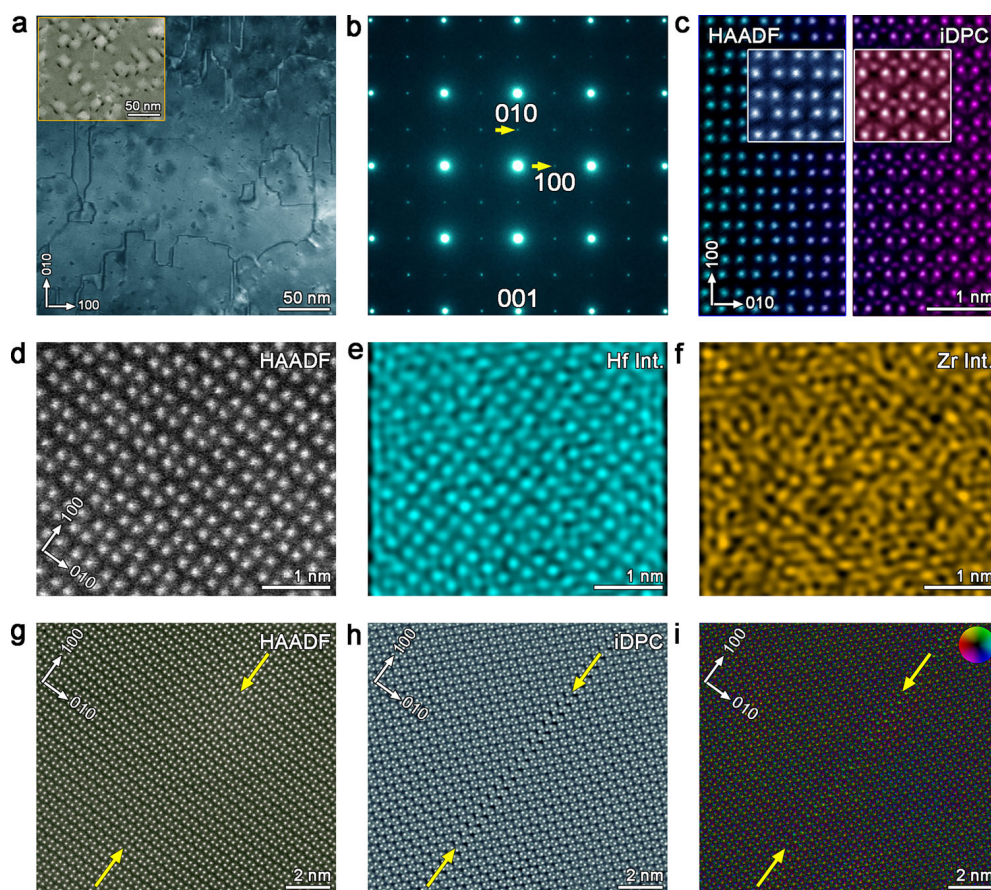


Fig. 3 | Antiphase domain boundaries in single-crystal HZO film. a Dark-field TEM image with the high-density domain boundaries. Inset is the low-magnification HAADF-STEM image, suggesting the manner of columnar-like growth. **b** SAED pattern of the HZO film along the [001] zone axis. **c** Atomic-resolved HAADF-STEM (left panel) and iDPC-STEM (right panel) images of the monoclinic HZO. Insets are the zoom-in HAADF-STEM and iDPC-STEM images displaying the detailed

distribution of Hf/Zr- and O- atomic columns. **d–f** HAADF-STEM image and corresponding EDXS elemental maps of Hf- and Zr- atomic columns. **g** Atomic-resolved HAADF-STEM image in which an antiphase domain boundary is marked with a pair of arrows. **h** iDPC-STEM image corresponding to the area in (g), oxygen ions are visualized. **i** DPC-STEM image, showing electric field modulation at the antiphase domain boundary.

manner (inset in Fig. 3a), and the high-density domain boundaries in the single-crystalline HZO films might be derived from the column coalescence during the film growth^{42–44}. The monoclinic lattice of the films is further supported by [001] EDP (Fig. 3b) acquired by slightly tilting the film normal. In order to figure out the lattice distortions particularly at the domain boundary, multimode imaging techniques which include integrated differential phase contrast (iDPC)-STEM and differential phase contrast (DPC)-STEM are alternatively applied together with the high angle angular dark-field (HAADF)-STEM to display all the elements at the atomic scale. The contrast in the iDPC-STEM image is approximately linear to the atomic number, which is helpful for simultaneously imaging heavy and light elements. Besides, the DPC-STEM technique could directly provide the electric field at the atomic scale^{45,46}. Accordingly, the projections of Hf/Zr and O atomic columns along [001] direction of the monoclinic phase are clearly imaged at the atomic scale (Fig. 3c), and alternatively, atomic-resolved Hf/Zr arrays are visualized in the HAADF image and composition maps with single element (Fig. 3d–f). Although the domain boundaries in the monoclinic HZO phase are hard to be discernible in the HAADF-STEM image (Fig. 3g), they emphasize themselves as the antiphase domain boundary (APB) in the iDPC-STEM image (Fig. 3h). Contrast resultant from the structural distortion at the APB is also remarkable in the DPC-STEM image (Fig. 3i).

The high-density APBs in HZO films are schematically illustrated in Fig. 4a. Two manually orthogonal directions namely [001] and [100], both of which are parallel to the boundary plane, are selected for

imaging the Hf/Zr and O atomic distribution at the domain boundary. According to the zoom-in HAADF-STEM (Fig. 4b) and iDPC-STEM (Fig. 4c) images along the [001] direction, the projection of the structural unit features the trapezoid-like (marked in yellow) and inverted trapezoid-like (marked in green), and they are alternately stacked along [010] direction. However, the periodic stacking is interrupted at the domain boundary (highlighted by the yellow arrow pair). Furthermore, the O-atomic columns marked with small balls are clearly seen in the iDPC-STEM image, and the O-ionic displacements feature an alternative upward and downward array in the monoclinic phase, highlighted with green and red arrows (Fig. 4c). It is of interest to find that, at the domain boundary, the periodicity of O-ionic displacements is broken, leaving a paired O ions within the Hf/Zr sublattice. It is noted that the paired O ions are located at the non-central position of the four surrounding Hf/Zr ions. Similar imaging modes are also performed to focus on the antiphase boundary along the [100] zone axis (Fig. 4d–g). According to the experimental images, the atomic model of the antiphase boundary is constructed and the projections of the optimized atomic structure along the [001] and [100] zone axes are displayed in Fig. 4h and 4i, respectively. The domain boundary is characterized by a crystal translation of $(1/2)d_{100}$ in (010) plane projected along [001] zone axis (Figs. 4h) and $(1/2)d_{001}$ in (010) plane projected along [100] zone axis (Fig. 4i), respectively. As a result, in three dimensions the antiphase domain boundary is located in (010) plane with a crystal translation of half of the diagonal along [101] direction, which might induce structure modulation and even phase

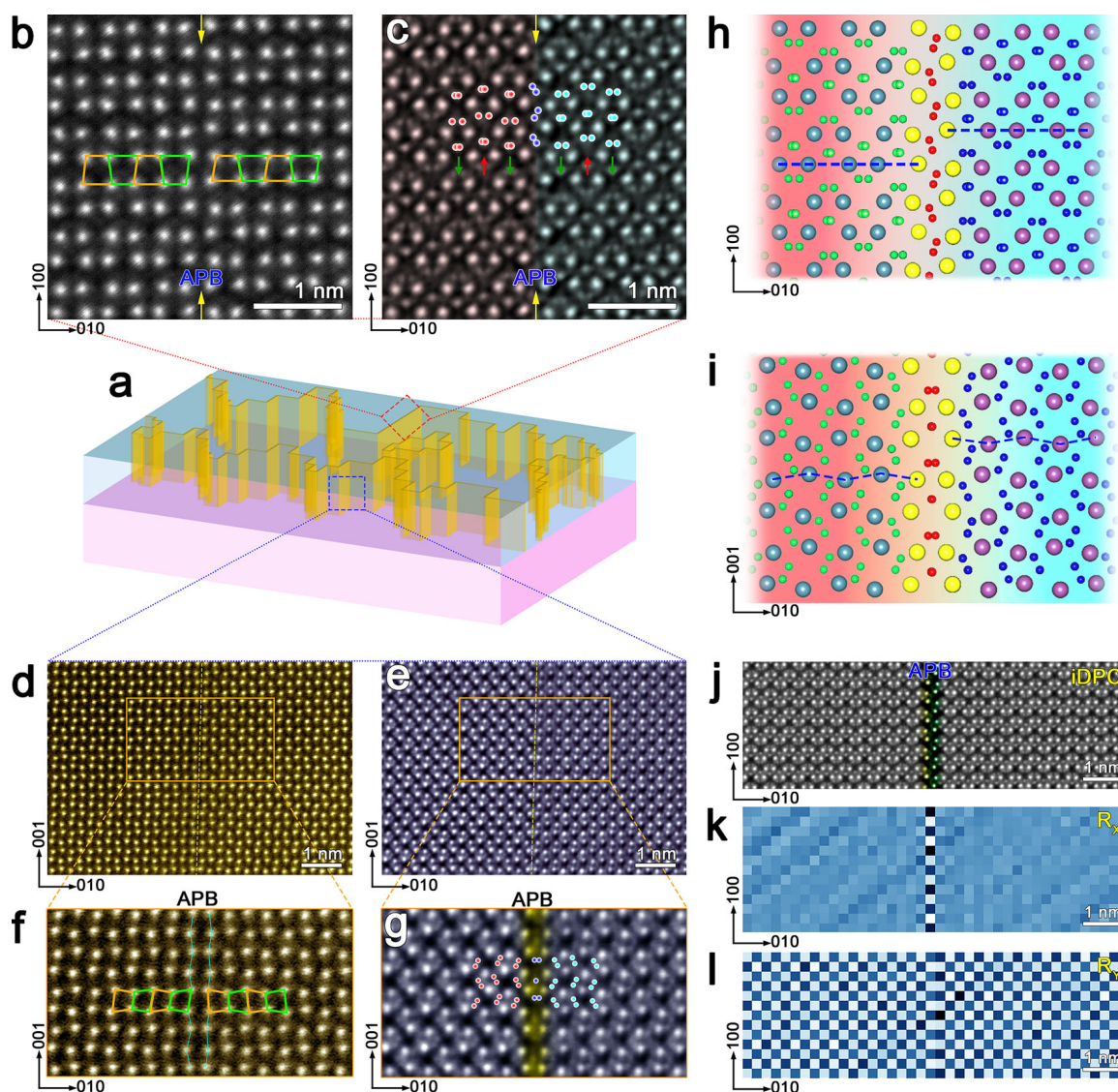


Fig. 4 | Atomic structure of the APBs in the HZO film. **a** Schematic illustration of the APBs in HZO film. **b, c** Planar-view atomic-resolved HAADF-STEM and iDPC-STEM images in which an APB is arrowed in yellow. Green and red arrows in (c) denoting the O-ionic displacements. **d, e** Cross-sectional atomic-resolved HAADF-STEM and iDPC-STEM images, an APB is located in the central area of this image. **f, g** Zoom-in HAADF-STEM and iDPC-STEM images of the yellow rectangles in (d) and (e). Atomic structure of the APB derived from the first-principles calculations, along the [001] and [100] zone axis, respectively. Blue dashed lines across the APB

in (h, i) highlight the APB-induced atomic displacement; Green, blue and red balls indicate the O-atomic columns in left domain, right domain and antiphase boundary, respectively; Grey, purple and yellow balls denote the Hf/Zr atomic columns in left domain, right domain and antiphase boundary, respectively. **j**, Cross-sectional atomic-resolved iDPC-STEM image of the antiphase boundary. **k, l** In-plane lattice rotation (R_x) and out-of-plane lattice rotation (R_y) corresponding to the area in (j). Lattice modulation is revealed based on the R_x and R_y maps.

transitions⁴⁷. Based on the HAADF-STEM (Supplementary Fig. 18a) and geometric phase analysis (GPA)^{48–50}, remarkable shear strain is revealed at the APB (Supplementary Fig. 18b). Furthermore, based on the atomic-resolved HAADF-STEM image, the position of each atomic column can be measured by fitting the atomic columns as 2D Gaussian peaks^{51–53}. By doing so, the lattice rotations along both in-plane and out-of-plane directions are acquired as shown in Fig. 4j–l. In a word, despite the non-polar nature of the monoclinic HZO phase, it is the formation of APB that leads to local lattice distortion and the symmetry breaking from the centrosymmetric to a polar variant.

In addition to the single APB as discussed in Fig. 4, repeated (010) APBs at the unit-cell level are frequently observed in the present study, showing a lamella structure embedded in the non-polar monoclinic phase. The thickness of the lamella corresponds to 2, 3, 4, 5, and 8 unit cells as seen in Fig. 5a–e. The localized structures in the lamella are modulated because of the APB-induced atomic displacement, as

revealed in the R_x maps in Fig. 5f–j. Thus, the Hf/Zr and O sublattices in the lamella are different from their counterparts in the monoclinic matrix, as highlighted in Fig. 5k, l. According to the polar character at the single APB, the expansion of APBs with the step of unit cell is expected to result in a polar variant (APB phase) with a specific symmetry. Taking a lamella with thickness of 8 unit cells as an example, the APB-stabilized phase is shown in the iDPC-STEM image (Fig. 5m), which displays the different Hf/Zr sublattice characters from the polar orthorhombic phase (Supplementary Figs. 19, 20). The reversed O-displacement vector map (Fig. 5n), extracted from the iDPC-STEM image in Fig. 5m, clearly exhibit the polar state along the [001] direction. To illuminate the symmetry of this polar variant, imaging along the [010] zone axis is carried out, as shown in Supplementary Fig. 21a. The intergrowth of the polar variant and monoclinic matrix is displayed in the atomic-resolved iDPC-STEM images, as shown in Supplementary Fig. 21b. Region 1 and 2 marked in Supplementary Fig. 21b

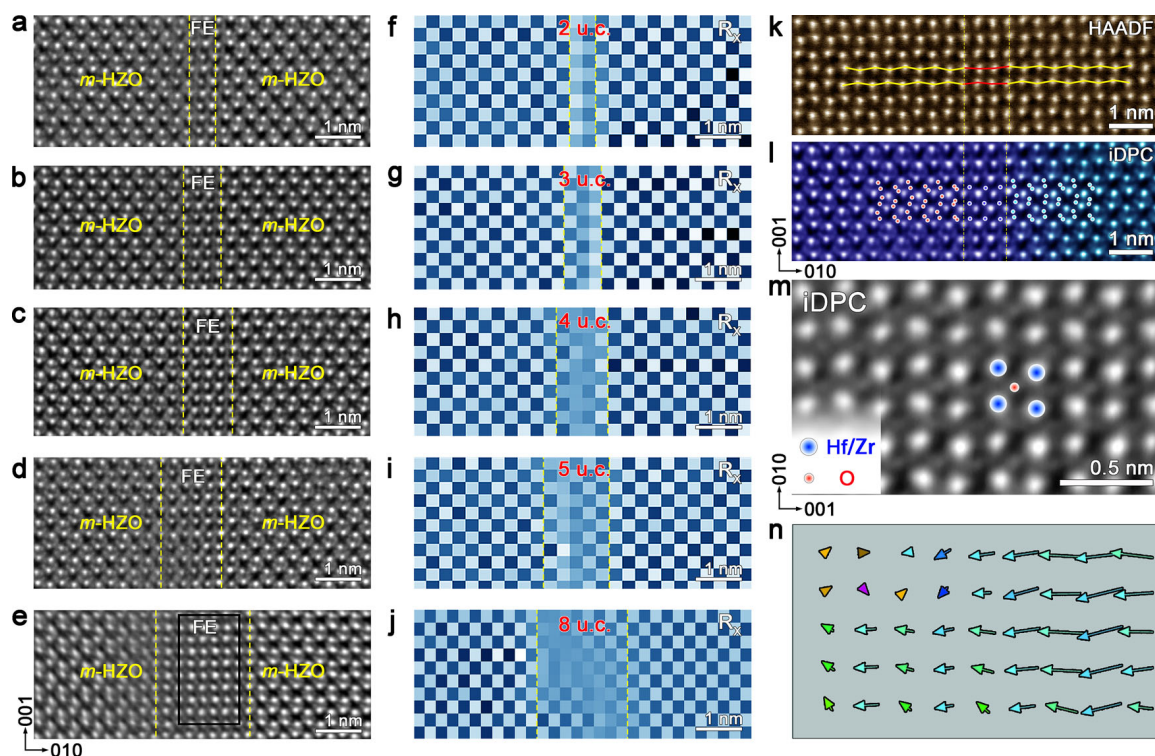


Fig. 5 | Expansion of antiphase boundaries in the HZO film. a–e Cross-sectional atomic-resolved iDPC-STEM images showing the intergrowth of the polar variant with the *m*-HZO phase. The polar variants feature lamella with thickness of 2 u.c., 3 u.c., 4 u.c., 5 u.c. and 8 u.c., respectively. **f–j** The R_x maps corresponding to (a–e). **k, l** Enlarged HAADF-STEM and iDPC-STEM images of the 3 u.c. antiphase boundary,

giving the detailed distribution of Hf/Zr- and O- atomic columns. **m, n** Enlarged iDPC-STEM image of the FE-HZO phase (black rectangle in (e)) and corresponding reversed O-displacement vector map, suggesting the ferroelectric displacements in FE-HZO.

correspond to the monoclinic phase ($P2_1/c$) of the matrix and the new polar variant, respectively. It is noted that the new polar variant features the same β angle with the $P2_1/c$ phase (Supplementary Fig. 21c, d), suggesting that it is a monoclinic phase as well.

According to the atomic mapping, the difference of Hf atomic chains in the APB phase and those in monoclinic phase is remarkable. In addition, the zigzag characteristic of the Hf atomic chains parallel to the APB in the APB phase is similar to that in the monoclinic phase. Thus, a new structural variant of HfO_2 is built by setting the coordinates of Hf atoms in the [010] direction to be $y = 0.25$ and $y = 0.75$, as shown in Supplementary Fig. 22a. By fixing the y coordinates of Hf atoms and optimizing the positions of O atoms, the resultant structure is still non-polar monoclinic, as shown in Supplementary Fig. 22b. It is seen that there are two O columns inside a parallelogram of four Hf atomic columns (see the shaded parallelogram in Supplementary Fig. 22b), while the experimental images suggest that there is only one O atomic column, as shown in Fig. 5l, m. Inspired by the experimental observations, O vacancies are introduced in this structure sequentially and the most stable structures at different vacancy concentrations are presented in Supplementary Fig. 22c–f. The atomic configurations shown in Supplementary Fig. 22f could be assigned a polar phase with the space group of Pc . This is consistent with the monoclinic nature of the polar variant revealed in Supplementary Fig. 21. The role of oxygen vacancies on stabilizing the APB-derived monoclinic polar variant is also confirmed by the increased volume of APBs by growing and annealing the HZO films at the low oxygen partial pressure of 10^{-6} Torr (Supplementary Fig. 23). This strategic manipulation of APB proportion would not only enhance the remanent polarization in ferroelectricity measurement but also demonstrate promising technological implications for non-volatile memory applications. It is worthwhile to add that repeated stacking faults in (100) plane of a monoclinic phase, instead of the (010) in the present study, at the unit-cell level

could result in the formation of an orthorhombic variant in an AlCo alloy⁴⁷.

A series of interface models between this polar phase and the nonpolar monoclinic phase are constructed. The orientation relationship between the two phases is $(010)_p // (010)_M$, $[100]_p // [100]_M$ and $[001]_p // [001]_M$, where the subscripts P and M represent the polar and monoclinic phases. As shown in Supplementary Fig. 24, the thickness of the nonpolar monoclinic phase is fixed and the thickness of the polar phase varies from 2 u.c. to 8 u.c. By calculating the formation energy of the interface model, it is found that with the increase of the APB width, the interfacial energy decreases, which means the influence of the interface on the APB phase decrease, as shown in Supplementary Fig. 25. In other words, the stability of the APB phase increase with the increase of the APB width. We also studied the stability of the APB phase from the perspective of clamping. By optimizing all lattice parameters of the APB phase, it is found the structure becomes a non-polar phase ($a = b = 4.858 \text{ \AA}$, $c = 5.062 \text{ \AA}$, $P4_2/mmc$), which indicates that the clamping of the monoclinic phase is important for the stabilization of the APB phase. The optimized atomic structures are shown in Fig. 6 and Supplementary Fig. 26. Based on these atomic structural models, high resolution images under the HAADF-STEM (Fig. 6d–f and Supplementary Fig. 26c, d) and ABF-STEM mode (Fig. 6g–i and Supplementary Fig. 26e, f) are simulated using the software of Dr. probe⁵⁴. As shown in Fig. 6g–i and Supplementary Fig. 26e, f, the images highlighted in yellow correspond to O-displacement vector maps in the APB phase. Furthermore, in addition to the experimental investigations in Fig. 2a, b, the switching of the stabilized polar monoclinic phase (Fig. 7a) is also studied by the nudged elastic band (NEB) method. The switching barrier is approximately 0.077 eV/u.c. (Fig. 7b), which is only 23% of that of the metastable polar orthorhombic phase (about 0.338 eV/u.c.). We also calculated the switching barrier of the interface model, taking the case of the APB width of 2 u.c. as an

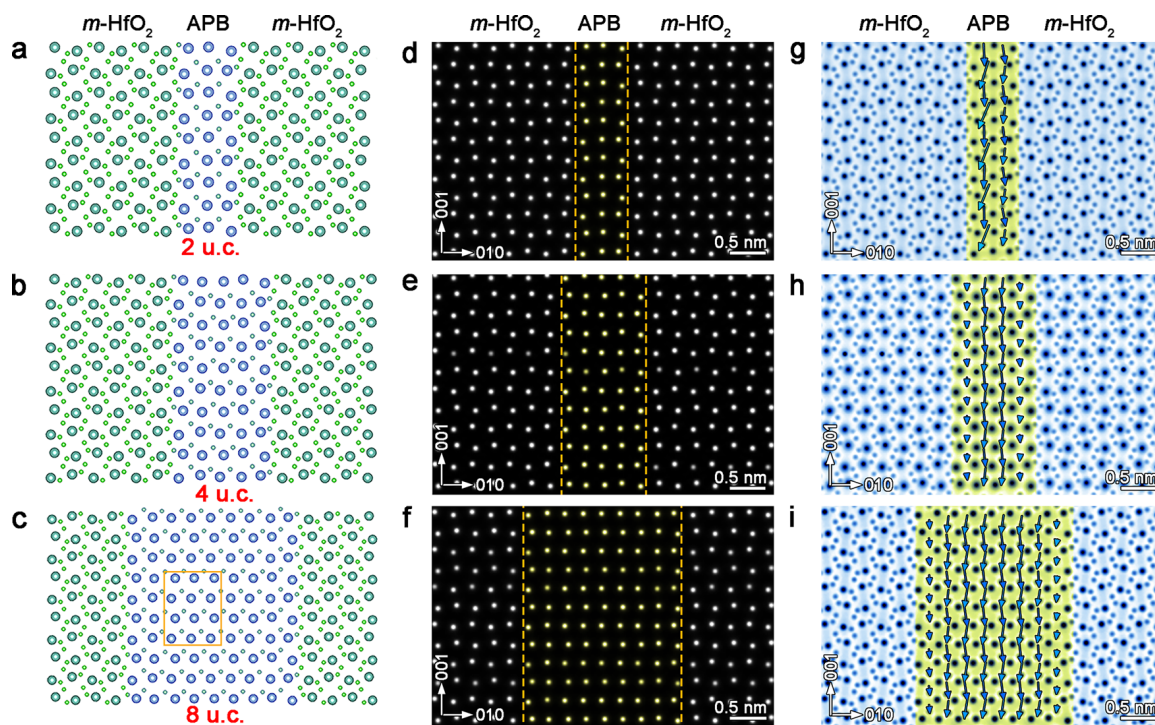


Fig. 6 | DFT calculations and STEM simulations revealing the stabilization of the polar phase at the APBs in m -HfO₂. **a–c** Atomic structure models of the APB in HfO₂ obtained by DFT structural relaxation, with the APB width of 2 u.c., 4 u.c., and

8 u.c., respectively. **d–f** HAADF images simulated by using the atomic structure models in (a–c). **g–i** ABF images simulated by using the atomic structure models in (a–c) and corresponding O-displacement vector maps at the APBs.

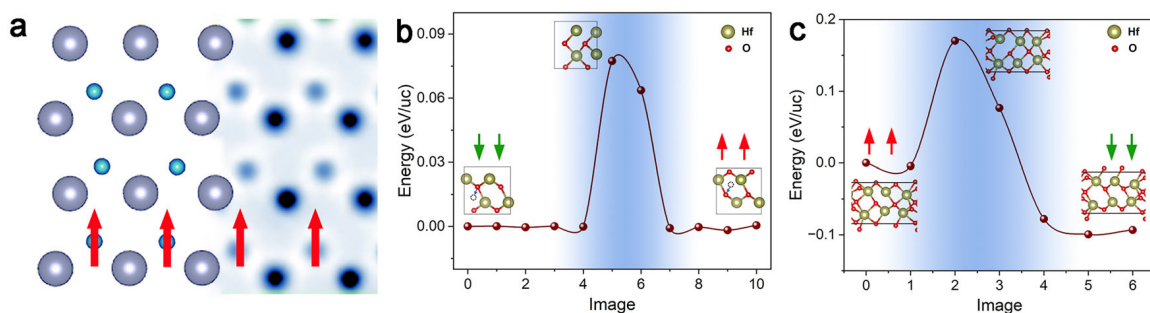


Fig. 7 | DFT calculations of the ferroelectricity for the polar phase at APBs. **a** Enlarged atomic structure models of the yellow rectangle in Fig. 6c (left panel) and simulated ABF image (right panel), red arrows suggesting the O-displacement vectors. **b** Switching barrier of the unit cell of the APB phase determined by DFT

calculations. **c** Switching barrier of the APB phase in the interface model with the APB width of 2 u.c. determined by DFT calculations. The red and green arrows denoting the upward and downward polarization, respectively.

example. As shown in Fig. 7c, the switching barrier is 0.170 eV/u.c., which is about 50% of that of the orthorhombic phase. Thus, the polar variant at the extended APB regions could be switched under a smaller coercive field, which is promising for the application in lower energy-cost memory devices.

In summary, we find the robust ferroelectricity in the monoclinic Hf_{0.5}Zr_{0.5}O₂ single-crystalline films, which is derived from the new polar monoclinic variant with the space group of Pc intergrown with the stable non-polar monoclinic phase ($P2_1/c$). The structural nature of the polar state is resultant from the lattice distortion at the antiphase boundary, which features a translation vector of half of the diagonal along [101] direction on the (010) plane of the nonpolar monoclinic phase. The constraint of the lattice distortion at the APBs makes the symmetry breaking from the centrosymmetric to the polar variant, in which oxygen vacancies play critical roles. The new polar phase is derived by introducing repeated antiphase boundaries at the unit-cell level in the monoclinic phase, which features robust polarization displacement. The intergrowth of the polar and non-polar phase makes the as-grown films feature the ferroelectric switching under an

external electric field with the high endurance of wake-up free and non-fatigue up to 10¹² cycles. The switching barrier for the stable polar variant is only 20%–50% of that for the metastable polar orthorhombic phase. Development of future electronic devices requires thin film with single-crystalline structure for the need of controllability and stability of the physical performance in the functional units, consequently, this study provides a new approach for obtaining robust ferroelectricity via engineering planar APBs in single-crystalline hafnium oxide, which would be helpful for developing silicon-compatible ferroelectric electronic devices such as ultra-dense and nonvolatile ferroelectric random-access memory.

Methods

Film deposition details

Using a Coherent CompPex PRO 201 F KrF excimer laser ($\lambda = 248$ nm) for pulsed laser deposition, a set of epitaxial Hf_{0.5}Zr_{0.5}O₂ thin films were grown on YSZ (001) substrates. The YSZ (001) substrates employed were commercially sourced without additional chemical or thermal processing. Prior to the deposition of Hf_{0.5}Zr_{0.5}O₂ thin films, the

substrates were heated to 900 °C and held at this temperature for 20 minutes to ensure surface cleanliness, followed by cooling to the deposition temperature of 850 °C at a rate of 5 °C·min⁻¹. The Hf_{0.5}Zr_{0.5}O₂ layers were deposited using a solid sintered target of the same composition, which was pre-sputtered for 20 minutes to remove surface contaminants. During film growth, the following parameters were applied: a repetition rate of 2 Hz, a substrate temperature of 850 °C, an oxygen partial pressure of 70 mTorr, and a laser energy density of 2 J·cm⁻². Subsequently, the as-deposited films were subjected to post-deposition annealing at 850 °C under an oxygen partial pressure of 200 Torr for 20 minutes, followed by slow cooling to room temperature at a rate of 5 °C·min⁻¹. Another Hf_{0.5}Zr_{0.5}O₂ films with increased volume of APBs were grown under the same conditions, apart from being grown and annealed at low oxygen partial pressure of 10⁻⁶ Torr.

XRD structural analysis

X-ray θ - 2θ scan, rocking curve, and reciprocal space mappings were performed using a high-resolution X-ray diffraction with Cu K α 1 radiation in a X'Pert3 MRD diffractometer (Malvern Panalytical).

TEM sample preparation, TEM/STEM observations

Cross-sectional and planar-view TEM specimens for both TEM and STEM observations were prepared through a conventional procedure of sample preparation involving slicing, bonding, mechanical polishing, dimpling, and final ion milling. Ion milling was performed using a Gatan 695 PIPS system with an initial low angle (5°) and cooling stage, followed by a final polishing step at 0.3 kV for 10 minutes to minimize ionic beam-induced damage. The SAED and bright-field TEM imaging were carried out on a JEOL JEM-F200 transmission electron microscope operating at 200 kV. The HAADF-STEM, iDPC-STEM, and DPC-STEM images were acquired using a ThermoFisher Spectra 300 X-FEG aberration-corrected STEM equipped with dual Cs correctors and a monochromator, operated at 300 kV.

STEM result analyses

Strain analyses were performed based on the method of GPA⁴⁷, which was carried out using Gatan Digital Micrograph software. The atomic positions of Hf/Zr and O were precisely determined through two-dimensional Gaussian peak fitting implemented in Matlab⁵². This approach enabled accurate measurement of the in-plane and out-of-plane rotations of Hf/Zr sublattices, as well as the displacement of oxygen ions. To improve signal quality, the HAADF-STEM and iDPC-STEM images were preprocessed using a Wiener filter and a low-pass annular mask conforming to the instrument's resolution limit, both applied to suppress noise.

AFM observations

The local AFM observations were carried out on a commercial AFM system (Asylum Research Cypher ES) at room temperature. The single-frequency mode was used to acquire the topography image of the HZO film. The probes used were Ti/Ir (5/20) coated tips (ASYLEEC-01-R) with nominal $k=2.8$ N m⁻¹. Polarization switching of the HZO films were observed using a commercial piezoresponse force microscope (Cypher ES, Asylum Research, US) in the dual AC resonance tracking (DART) mode. Conductive Pt/Ir-coated silicon cantilevers (NANO WORLD, ARROW-EFM) were used for PFM hysteresis loop measurements, with the resonance frequency being 75 kHz and the force constant being ~ 2.8 N m⁻¹.

First-principles calculations

We have carried out first-principles calculations in the framework of density functional theory as implemented in the Vienna ab-initio simulation package (VASP)^{55,56}. The Perdew-Burke-Ernzerhof

functional⁵⁷ was used as the exchange-correlation functional for all calculations. The plane wave cutoff energy was set to be 500 eV. The Monkhorst-Pack k-point meshes of 8 × 8 × 8 was adopted for the monoclinic and APB phases and for the interface models containing the APB, the k-point mesh of 8 × 8 × 1 was adopted. The convergence conditions for the electronic self-consistent and the ionic relaxation loops were set to be 10⁻⁴ eV and 5 meV·Å⁻¹, respectively. The interface energies of the interface models are calculated by the following equation:

$$E_{int} = (E_{total} - nE_P - mE_M) / 4S$$

where E_{total} is the total energies of the interface model, E_P and E_M are the total energies of the unit cells of the polar phase and the monoclinic phase, n and m are the numbers of the unit cells of the polar phase and the monoclinic phase in the interface model, and S is the cross-sectional area of the interface model. The factor 4 appears in the denominator since there exist four interfaces in the model.

STEM simulation

The simulated HAADF-STEM and ABF-STEM images were obtained using Dr. Probe based on the multislice method⁵⁴. During the STEM simulation, an acceleration of 300 kV, a Cs of 0.01 nm, a source size of 0.04 nm, a probe convergence angle of 24 mrad, and collection semiangles of 80–250 mrad for HAADF detector and 11–24 mrad for the ABF detector were used. Partially coherent probe intensity was chosen as the display function. The supercells with the dimensions of 6.85428 nm × 4.4070 nm × 8.82084 nm were used for the series of extended APBs models constructed via DFT calculations.

Ferroelectricity Measurements

The in-plane interdigitated Ti/Au (10 nm/100 nm) electrodes were patterned on the HZO film using a designed shadow mask by an electric beam evaporator (ULVAC ei-501z). The spacing between the adjacent electrodes was 7 μ m, with the width of the interdigital electrodes at 3 μ m. The in-plane ferroelectric properties of the film systems were measured by a Keithley 4200A-SCS semiconductor device parameter analyzer at room temperature. The bipolar triangular waveform was applied to obtain the in-plane P - E (P - V) curves of the HZO films. The polarization values in the P - E (P - V) curves were calculated using the charge, the area of the electrode, and the proportion of the polar monoclinic phase in the HZO film. The I - t curves were obtained using the PUND measurement, with the five sequential rectangular pulses being applied: an initial negative pulse followed by two positive pulses and two negative pulses.

Data availability

The data that support the findings of this study are provided in the article and the Supplementary Information. The data sets generated and analyzed during the current study are available from the corresponding author on reasonable request.

References

1. Junquera, J. & Ghosez, P. Critical thickness for ferroelectricity in perovskite ultrathin films. *Nature* **422**, 506–509 (2003).
2. Ambriz-Vargas, F. et al. A complementary metal oxide semiconductor process-compatible ferroelectric tunnel junction. *ACS Appl. Mater. Interfaces* **9**, 13262–13268 (2017).
3. Boscke, T. S., Muller, J., Brauhaus, D., Schroder, U. & Bottger, U. Ferroelectricity in hafnium oxide thin films. *Appl. Phys. Lett.* **99**, 102903 (2011).
4. Cheema, S. S. et al. Enhanced ferroelectricity in ultrathin films grown directly on silicon. *Nature* **580**, 478–482 (2020).
5. Jo, S. et al. Negative differential capacitance in ultrathin ferroelectric hafnia. *Nat. Electron.* **6**, 390–397 (2023).

6. Schroeder, U., Park, M. H., Mikolajick, T. & Hwang, C. S. The fundamentals and applications of ferroelectric HfO₂. *Nat. Rev. Mater.* **7**, 653–669 (2022).
7. Cheema, S. S. et al. Ultrathin ferroic HfO₂–ZrO₂ superlattice gate stack for advanced transistors. *Nature* **604**, 65–71 (2022).
8. Lee, H.-J. et al. Scale-free ferroelectricity induced by flat phonon bands in HfO₂. *Science* **369**, 1343–1347 (2020).
9. Cheema, S. S. et al. Emergent ferroelectricity in subnanometer binary oxide films on silicon. *Science* **376**, 648–652 (2022).
10. Yu, L., Zhao, H. J., Chen, P., Bellaïche, L. & Ma, Y. The anti-symmetric and anisotropic symmetric exchange interactions between electric dipoles in hafnia. *Nat. Commun.* **14**, 8127 (2023).
11. Ma, L.-Y. & Liu, S. Structural polymorphism kinetics promoted by charged oxygen vacancies in HfO₂. *Phys. Rev. Lett.* **130**, 096801 (2023).
12. Zhong, H. et al. Large-scale Hf_{0.5}Zr_{0.5}O₂ membranes with robust ferroelectricity. *Adv. Mater.* **34**, 2109889 (2022).
13. Yun, Y. et al. Intrinsic ferroelectricity in Y-doped HfO₂ thin films. *Nat. Mater.* **21**, 903–909 (2022).
14. Wang, Y. et al. A stable rhombohedral phase in ferroelectric Hf(Zr)_{1-x}O₂ capacitor with ultralow coercive field. *Science* **381**, 558–563 (2023).
15. Shimizu, T. et al. Growth of epitaxial orthorhombic YO_{1.5}-substituted HfO₂ thin film. *Appl. Phys. Lett.* **107**, 032910 (2015).
16. Katayama, K. et al. Orientation control and domain structure analysis of {100}-oriented epitaxial ferroelectric orthorhombic HfO₂-based thin films. *J. Appl. Phys.* **119**, 102903 (2016).
17. Li, T. et al. Epitaxial ferroelectric Hf_{0.5}Zr_{0.5}O₂ thin film on a buffered YSZ substrate through interface reaction. *J. Mater. Chem. C* **6**, 9224–9231 (2018).
18. Torrejón, L. et al. Growth and structural characterization of strained epitaxial Hf_{0.5}Zr_{0.5}O₂ thin films. *Phys. Rev. Mater.* **2**, 013401 (2018).
19. Shi, S. et al. Interface-engineered ferroelectricity of epitaxial Hf_{0.5}Zr_{0.5}O₂ thin films. *Nat. Commun.* **14**, 1780 (2023).
20. Kelley, K. P. et al. Ferroelectricity in hafnia controlled via surface electrochemical state. *Nat. Mater.* **22**, 1144–1151 (2023).
21. Kang, S. et al. Highly enhanced ferroelectricity in HfO₂-based ferroelectric thin film by light ion bombardment. *Science* **376**, 731–738 (2022).
22. Mimura, T. et al. Effects of heat treatment and in situ high-temperature X-ray diffraction study on the formation of ferroelectric epitaxial Y-doped HfO₂ film. *Jpn. J. Appl. Phys.* **58**, SB09 (2019).
23. Mimura, T., Shimizu, T., Uchida, H. & Funakubo, H. Room-temperature deposition of ferroelectric HfO₂-based films by the sputtering method. *Appl. Phys. Lett.* **116**, 062901 (2020).
24. Müller, J. et al. Ferroelectricity in simple binary ZrO₂ and HfO₂. *Nano Lett.* **12**, 4318–4323 (2012).
25. Shen, Z. et al. Epitaxial growth and phase evolution of ferroelectric La-doped HfO₂ films. *Appl. Phys. Lett.* **120**, 162904 (2022).
26. Liu, S. & Hanrahan, B. M. Effects of growth orientations and epitaxial strains on phase stability of HfO₂ thin films. *Phys. Rev. Mater.* **3**, 054404 (2019).
27. Nukala, P. et al. Reversible oxygen migration and phase transitions in hafnia-based ferroelectric devices. *Science* **372**, 630–635 (2021).
28. Materlik, R., Künneth, C. & Kersch, A. The origin of ferroelectricity in Hf_xZr_{1-x}O₂: a computational investigation and a surface energy model. *J. Appl. Phys.* **117**, 134109 (2015).
29. Zhao, D., Chen, Z. & Liao, X. Microstructural evolution and ferroelectricity in HfO₂ films. *Microstructures* **2**, 2022007 (2022).
30. Hadnagy, T. Materials and production characterization requirements for the production of FRAM® memory products. *Integr. Ferroelectr.* **18**, 1–17 (1997).
31. Loke, W. K., Yoon, S. F. & Ng, T. K. and, S.Z., Reciprocal space mapping of GaN_xAs_{1-x} grown by RF plasma-assisted solid source molecular beam epitaxy. *J. Cryst. Growth* **243**, 427–431 (2002).
32. Cho, J. W. et al. Atomic layer deposition of epitaxial ferroelectric Hf_{0.5}Zr_{0.5}O₂ thin films. *Adv. Funct. Mater.* **34**, 2314396 (2024).
33. Kashir, A., Kim, H., Oh, S. & Hwang, H. Large remnant polarization in a wake-up free Hf_{0.5}Zr_{0.5}O₂ ferroelectric film through bulk and interface engineering. *ACS Appl. Electron. Mater.* **3**, 629–638 (2021).
34. M. G. Kozodaev, et al. Mitigating wakeup effect and improving the endurance of ferroelectric HfO₂-ZrO₂ thin films by careful La-doping. *J. Appl. Phys.* **125**, 034101.034101-034101.034110 (2019).
35. Chen, H.-H. et al. Ferroelectric polarization enhancement in hafnium-based oxides through capping layer engineering. *IEEE J. Electron Devices Soc.* **10**, 947–952 (2022).
36. Zhou, D. et al. Wake-up effects in Si-doped hafnium oxide ferroelectric thin films. *Appl. Phys. Lett.* **103**, 192904 (2013).
37. Choi, Y. et al. Impact of chamber/annealing temperature on the endurance characteristic of Zr:HfO₂ ferroelectric capacitor. *Sensors* **22**, 4087 (2022).
38. Liu, H. et al. Structural and ferroelectric properties of Pr doped HfO₂ thin films fabricated by chemical solution method. *J. Mater. Sci.: Mater. Electron.* **30**, 5771–5779 (2019).
39. Liu, L. et al. Large ferroelectric polarization and high dielectric constant in HfO₂-based thin films via Hf_{0.5}Zr_{0.5}O₂/ZrO₂ nanobilayer engineering. *J. Materiom.* **11**, 100922 (2024).
40. Li, S. et al. Involvement of unsaturated switching in the endurance cycling of Si-doped HfO₂ ferroelectric thin films. *Adv. Electron. Mater.* **6**, 2000264 (2020).
41. Chen, K.-T. et al. Improvement on ferroelectricity and endurance of ultra-thin HfZrO₂ capacitor with molybdenum capping electrode. *Electron Devices Technol. Manuf. Conf. (EDTM)* **62**, 64 (2019).
42. E. Palstra, H. Celotto, Origin of the increased resistivity in epitaxial Fe₃O₄ films. *Phys. Rev. B* **66**, 201101 (2002).
43. Gilks, D., Lari, L., Matsuzaki, K., Hosono, H. & Susaki, T. Structural study of Fe₃O₄(111) thin films with bulk like magnetic and magnetotransport behaviour. *J. Appl. Phys.* **115**, 17C107–101C107 (2014). 117C107-103.
44. McKenna, K. P. et al. Atomic-scale structure and properties of highly stable antiphase boundary defects in Fe₃O₄. *Nat. Commun.* **5**, 5740 (2014).
45. Shibata, N. et al. Differential phase-contrast microscopy at atomic resolution. *Nat. Phys.* **8**, 611–615 (2012).
46. Wang, W. et al. Direct atomic-scale structure and electric field imaging of triazine-based crystalline carbon nitride. *Adv. Mater.* **33**, e2106359 (2021).
47. Li, X. Z., Ma, X. L. & Kuo, K. H. A structural model of the orthorhombic Al₃Co derived from the monoclinic Al₁₃Co₄ by high-resolution electron microscopy. *Philos. Mag. Lett.* **70**, 221–229 (2006).
48. Hytch, M. J., Snoeck, E. & Kilaas, R. Quantitative measurement of displacement and strain fields from HREM micrographs. *Ultra-microscopy* **74**, 131–146 (1998).
49. Geng, W. et al. Atomic-scale tunable flexoelectric couplings in oxide multiferroics. *Nano Lett.* **21**, 9601–9608 (2021).
50. Tang, Y. L., Zhu, Y. L., Liu, Y., Wang, Y. J. & Ma, X. L. Giant linear strain gradient with extremely low elastic energy in a perovskite nanostructure array. *Nat. Commun.* **8**, 15994 (2017).
51. Geng, W. R. et al. Rhombohedral-orthorhombic ferroelectric morphotropic phase boundary associated with a polar vortex in BiFeO₃ films. *ACS Nano* **12**, 11098–11105 (2018).
52. Anthony, S. M. & Granick, S. Image analysis with rapid and accurate two-dimensional gaussian fitting. *Langmuir* **25**, 8152–8160 (2009).
53. Tang, Y. L. et al. Observation of a periodic array of flux-closure quadrants in strained ferroelectric PbTiO₃ films. *Science* **348**, 547–551 (2015).

54. Barthel, J. Dr. Probe: A software for high-resolution STEM image simulation. *Ultramicroscopy* **193**, 1–11 (2018). S0304399118301402.
55. Kresse, G. & Furthmüller, J. Efficiency of ab-initio total energy calculations for metals and semiconductors using a plane-wave basis set. *Comput. Mater. Sci.* **6**, 15–50 (1996).
56. Hafner, J. Materials simulations using VASP—a quantum perspective to materials science. *Comput. Phys. Commun.* **177**, 6–13 (2007).
57. Perdew, J. P. et al. Restoring the density-gradient expansion for exchange in solids and surfaces. *Phys. Rev. Lett.* **100**, 136406 (2008).

Acknowledgements

This work is supported by National Natural Science Foundation of China (NO. 52201018 (W.R.G.), NO. 52571013 (W.R.G.), NO. 51971223 (Y.L.Z.), NO. 51922100 (Y.L.T.), NO. 51901166 (S.R.Z.)), Guangdong Basic and Applied Basic Research Foundation (2021A1515110291 (W.R.G.), 2023A1515012796 (W.R.G.), 2024A1515140162 (W.R.G.)), Guangdong Provincial Quantum Science Strategic Initiative (GDZX2202001, GDZX2302001, GDZX2402001 (X.L.M.)), the Open Fund of the Microscopy Science and Technology, Songshan Lake Science City (202401202 (W.R.G.)), the Key Research Program of Frontier Sciences CAS (QYZDJ-SSW-JSCO10 (X.L.M.)). Y.J.W. acknowledges the Youth Innovation Promotion Association CAS (No. 2021187). Y.L.T. acknowledges the Scientific Instrument Developing Project of CAS (YJKYYQ20200066), and the Youth Innovation Promotion Association of CAS (Y202048).

Author contributions

W.R.G. and Y.J.W. contributed equally to this work. X.L.M. conceived the project on the architecture of quantum materials modulated by ferroelectric polarizations; W.R.G., Y.L.Z., and X.L.M. designed the sample structures and subsequent experiments. W.R.G. performed the thin-film growth, XRD, and PFM observations. W.R.G., Y.L.T. performed the TEM and STEM observations. W.R.G. performed the STEM simulations. Y.J.W. performed the first-principles calculations and digital analysis of the STEM data. S. Zhang, H. Ma, and S. Tuo performed the measurements of the ferroelectric property. All authors participated in the discussion and interpretation of the data.

Competing interests

The authors declare no competing interests.

Additional information

Supplementary information The online version contains supplementary material available at <https://doi.org/10.1038/s41467-025-63907-z>.

Correspondence and requests for materials should be addressed to Xiu-Liang Ma.

Peer review information *Nature Communications* thanks Minghua Tang, and the other anonymous reviewer(s) for their contribution to the peer review of this work. A peer review file is available.

Reprints and permissions information is available at <http://www.nature.com/reprints>

Publisher's note Springer Nature remains neutral with regard to jurisdictional claims in published maps and institutional affiliations.

Open Access This article is licensed under a Creative Commons Attribution-NonCommercial-NoDerivatives 4.0 International License, which permits any non-commercial use, sharing, distribution and reproduction in any medium or format, as long as you give appropriate credit to the original author(s) and the source, provide a link to the Creative Commons licence, and indicate if you modified the licensed material. You do not have permission under this licence to share adapted material derived from this article or parts of it. The images or other third party material in this article are included in the article's Creative Commons licence, unless indicated otherwise in a credit line to the material. If material is not included in the article's Creative Commons licence and your intended use is not permitted by statutory regulation or exceeds the permitted use, you will need to obtain permission directly from the copyright holder. To view a copy of this licence, visit <http://creativecommons.org/licenses/by-nc-nd/4.0/>.

© The Author(s) 2025



Full length article

Genetic inheritance relationship between ferroelectric skyrmion-bubble and 180° domain

Feng-Hui Gong^{a,b,1} , Yu-Ting Chen^{a,b,1} , Hui-Mei Li^{c,d} , Kang-Ming Luo^{c,d} , Meng-Jiao Han^a,
Yu-Jia Wang^{c,d} , Yun-Long Tang^{c,d,*} , Yin-Lian Zhu^{a,e,*} ,
Xiu-Liang Ma^{a,b,f,g} 

^a Bay Area Center for Electron Microscopy, Songshan Lake Materials Laboratory, Dongguan 523808 Guangdong, China

^b Institute of Physics, Chinese Academy of Sciences, Beijing 100190, China

^c Shenyang National Laboratory for Materials Science, Institute of Metal Research, Chinese Academy of Sciences, Shenyang 110016, China

^d School of Materials Science and Engineering, University of Science and Technology of China, Shenyang 110016, China

^e School of Materials Science and Engineering, Hunan University of Science and Technology, Xiangtan 411201, China

^f Quantum Science Center of Guangdong-HongKong-Macau Greater Bay Area, Shenzhen, China

^g State Key Lab of Advanced Processing and Recycling on Non-ferrous Metals, Lanzhou University of Technology, Lanzhou 730050, China

ARTICLE INFO

Keywords:

Skyrmion-bubble
Formation mechanism
Ferroelectric superlattice
Transmission electron microscopy
Phase-field simulation

ABSTRACT

Ferroelectric skyrmion-bubbles possess topological protection and exhibit novel functional properties, such as negative capacitance and high second harmonic generation performance, which hold promise for applications in nanoelectronic devices. From a theoretical perspective, the emergence of skyrmion-bubbles is generally attributed to the competition between elastic energy, gradient energy, electrostatic energy, and bulk energy. In this work, a series of PbTiO₃/SrTiO₃ (PTO/STO) superlattices with different thicknesses were grown on SrTiO₃ substrates by pulsed laser deposition (PLD) and investigated by both (scanning) transmission electron microscopy ((S)TEM) and phase field simulation. Based on the effect of strain engineering on domain configurations, and by comparing trivial and nontrivial domains as well as ferroelectric and ferroelastic domains, the experiment shows that skyrmion-bubbles originate from 180° ferroelectric domains. The symmetric STO layers sandwiching the PTO cause the depolarization field to re-segment the strip-like 180° domains in the PTO layers, leading to the evolution of 180° domains into skyrmion-bubbles. These results are expected to provide useful information for understanding the origin of ferroelectric skyrmion-bubbles and may advance research in ferroelectric physics.

1. Introduction

The topological structure in ferroelectric materials is based on dipoles or polarization as fundamental units[1–4], which differs from the spin-based topological structures found in magnetic materials. Recently, a series of topological domains, well-known in ferromagnets, have been directly observed at the atomic scale in ferroelectrics[5–13]. Among these, ferroelectric skyrmion-bubbles exhibit characteristics akin to both magnetic skyrmions and magnetic bubbles[14–16]. Furthermore, skyrmion-bubbles display chirality[14], negative capacitance[17], tunability dielectric permittivity, and high second harmonic generation performance[18], making them promising candidates for high-density memory and high-performances energy-harvesting devices in the

post-Moore era[19].

In 2010, synchrotron radiation results detected signals of ferroelectric skyrmion-bubbles[20]. However, transmission electron microscopy (TEM) was not employed to study the PbTiO₃/SrTiO₃ (PTO/STO) superlattice at that time, leading to the mistake belief that these structures were merely 180° domain[20], which delayed the discovery of the ferroelectric skyrmion-bubbles by a decade. This underscores the vital role of TEM in material science research and highlights the importance of using multiple experimental techniques to validate findings. It was not until 2019 that ferroelectric skyrmion-bubbles were experimentally observed in PTO/STO superlattices grown on STO substrates[14].

Next, a series of experimental and theoretical investigations were conducted on the phase transitions of skyrmion-bubbles[21–25].

* Corresponding authors.

E-mail addresses: yltang@imr.ac.cn (Y.-L. Tang), zhuyinlian@sslabs.org.cn (Y.-L. Zhu).

¹ These authors contributed equally to this work.

Electric fields can be create, annihilate, shrink, and expand polar skyrmion-bubbles, which can also undergo reversible topological phase transitions[21,22,25]. Upon heating, skyrmion-bubbles can form a meron intermediate state with the $-1/2$ topological charge[23]. Interestingly, skyrmion-bubbles can be maintained in ultrathin superlattices with limited thickness[15]. Additionally, first-principles-based simulations indicated that twisted light can drive dynamic polar skyrmions and transfer its nonzero winding number to ultrathin ferroelectric films[26].

Previous studies have focused on revealing the topological phase transition behavior of skyrmion-bubbles. However, there has been ongoing controversy regarding the origin of ferroelectric skyrmion-bubbles structures. From a theoretical perspective, the origin and topological phase transition behavior of ferroelectric skyrmion-bubbles are typically explained through the competition of different energy states. Additionally, the strain state of ferroelectric skyrmion-bubbles remains unclear. In this work, we attempt to reveal the potential relationship between skyrmion-bubbles and 180° domains from the perspective of strain, and to clarify the origin of skyrmion-bubbles based on the depolarization field.

2. Experimental details

2.1. Sample preparation using pulsed-laser deposition

$[(\text{PTO})_m/(\text{STO})_n]_n$ ($m = 12, 19, 23, 27, 37$ u.c., $n = 10$) superlattices were synthesized on STO substrates using PLD with a 248 nm KrF excimer laser. The PTO target consisted of 3 mol percent Pb-enriched sintered ceramics. Similarly, $[(\text{PTO})_m/(\text{STO})_n]_n$ ($m = 12$ u.c.) superlattices were also synthesized on DSO substrates via PLD. For the STO layer, a target made of sintered ceramics with a standard stoichiometric ratio was used. The cubic and orthogonal substrates were ultrasonically cleaned in acetone. The growth temperature and oxygen pressure for the PTO and STO layers were 700°C and 75 mtorr, respectively. Before deposition, the STO and GSO substrates were heated at 750°C for 5 min and then maintained at 700°C for growth. The PTO target was pre-sputtered for 5000 shots to clean the surface of substrate. During the growth of the superlattices, an oxygen pressure of 75 mTorr, a laser energy density of 2 J/cm^2 , and a repetition rate of 4 Hz were used. After deposition, the superlattices were stabilized at 700°C for 10 min and then cooled down to 200°C at a rate of $5^\circ\text{C}/\text{min}$ under an oxygen pressure of 2×10^2 Torr.

2.2. TEM and STEM sample preparation

Cross-sectional samples for TEM observations were prepared through a series of steps, including slicing, grinding, dimpling, and finally ion milling by using Gatan Precision Ion Polishing System (PIPS) 691. Unlike the cross-sectional samples, the planar view samples were milled exclusively from the substrate side to prevent damage to the film. During the initial stage of ion milling, the voltage was set to 8 kV with an ion beam incident angle of 9° . The voltage and incident angle were gradually reduced to 3 kV and 3° , respectively, in 20-minute steps, until colored stripes began to appear. The final ion-milling voltage was then reduced to 0.5 kV to minimize the formation of an amorphous layer caused by ion-beam damage[27,28].

2.3. TEM and STEM characterization

Diffraction contrast images were obtained using a Tecnai G2 F30 transmission electron microscope (FEI). Selected area electron diffraction patterns were captured with a JEOL 2010 high-resolution TEM. HAADF-STEM images were acquired using a Titan G2 60–300 microscope, which is equipped with a high-brightness field-emission gun and double aberration (Cs) correctors from CEOS, and operates at 300 kV. All atomic-scale HAADF-STEM images were drift-corrected and filtered to ensure clarity and accuracy.

2.4. Geometric phase analysis (GPA)

Large scale strain fields were deduced for the HAADF-STEM images using custom plugins of GPA for Gatan DigitalMicrograph[29–32].

2.5. Phase field simulation

The polarization distribution in the STO/PTO/STO film and the PTO film with STO as the substrate was studied by three dimensional (3D) phase field simulations. The adopted order parameters are the three components of the spontaneous polarization[33–35]. The system energy is composed of bulk, gradient, elastic, electrostatic ones:

$$F = \int_V [f_{\text{bulk}}(P_i) + f_{\text{grad}}(P_{i,j}) + f_{\text{elas}}(P_i, \varepsilon_{ij}) + f_{\text{elec}}(P_i, E_i)] dV \quad (1)$$

The first term is the bulk energy density:

$$f_{\text{bulk}} = \alpha_1 (P_1^2 + P_2^2 + P_3^2) + \alpha_{11} (P_1^4 + P_2^4 + P_3^4) + \alpha_{12} (P_1^2 P_2^2 + P_2^2 P_3^2 + P_1^2 P_3^2) + \alpha_{111} (P_1^6 + P_2^6 + P_3^6) + \alpha_{112} [P_1^4 (P_2^2 + P_3^2) + P_2^4 (P_1^2 + P_3^2) + P_3^4 (P_1^2 + P_2^2)] + \alpha_{123} P_1^2 P_2^2 P_3^2 \quad (2)$$

The second term is gradient energy density:

$$f_{\text{grad}} = \frac{1}{2} G_{11} (P_{1,1}^2 + P_{2,2}^2 + P_{3,3}^2) + G_{12} (P_{1,1} P_{2,2} + P_{2,2} P_{3,3} + P_{1,1} P_{3,3}) + \frac{1}{2} G_{44} [(P_{1,2} + P_{2,1})^2 + (P_{2,3} + P_{3,2})^2 + (P_{1,3} + P_{3,1})^2] \quad (3)$$

The third term is elastic energy density:

$$f_{\text{elas}} = \frac{1}{2} C_{ijkl} (\varepsilon_{ij} - \varepsilon_{ij}^0) (\varepsilon_{kl} - \varepsilon_{kl}^0) \quad (4)$$

where ε_{ij} is the total strain and ε_{ij}^0 is the spontaneous strain due to the paraelectric/ferroelectric phase transition. Their difference is the elastic strain. The spontaneous strain is related to the polarization by the electrostrictive coefficients:

$$\begin{aligned} \varepsilon_{11}^0 &= Q_{11} P_1^2 + Q_{12} (P_2^2 + P_3^2) \\ \varepsilon_{22}^0 &= Q_{11} P_2^2 + Q_{12} (P_2^2 + P_3^2) \\ \varepsilon_{33}^0 &= Q_{11} P_3^2 + Q_{12} (P_1^2 + P_2^2) \\ \varepsilon_{23}^0 &= Q_{44} P_2 P_3 \\ \varepsilon_{13}^0 &= Q_{44} P_1 P_3 \\ \varepsilon_{12}^0 &= Q_{44} P_1 P_2 \end{aligned} \quad (5)$$

The last term is the electrostatic energy density:

$$f_{\text{elec}} = -\frac{1}{2} \varepsilon_0 \varepsilon_b E_i^2 - E_i P_i \quad (6)$$

where ε_0 is the permittivity of vacuum and ε_b is the background relative dielectric constant.

The simulation size of the STO/PTO/STO films is $200\Delta x \times 200\Delta y \times 100\Delta z$ and the simulation size of the PTO film is $200\Delta x \times 200\Delta y \times 50\Delta z$. The grid sizes along the three axes are $\Delta x = \Delta y = 0.4\text{ nm}$ and $\Delta z = 0.2\text{ nm}$. In STO/PTO/STO film, the thickness of the STO layer and the PTO layer are 5 nm and 10 nm, respectively. The bottom STO layer is considered as the part of the substrate which is allowed to deform.

The periodic boundary condition is applied along the x and y directions. The mechanical boundary condition is a mixed one: the top surface of the film is in a traction-free state, while the bottom of the deformable region in the substrate is fixed. At the top and bottom surfaces of the simulation box, the short-circuit electric boundary condition is applied in the simulation. All material coefficients of PTO and STO are adopted from previous publication[33]. We assume that the equilibrium of mechanical stress and electrical field is much faster than the evolution

of domain structures. Thus, for each polarization configuration, the mechanical and electrical equilibrium equations are solved to obtain the corresponding driving force.

$$\sigma_{ij,j} = 0 \quad (7)$$

$$D_{i,i} = 0 \quad (8)$$

The evolution of polarization is governed by the time-dependent Ginzburg-Landau equation:

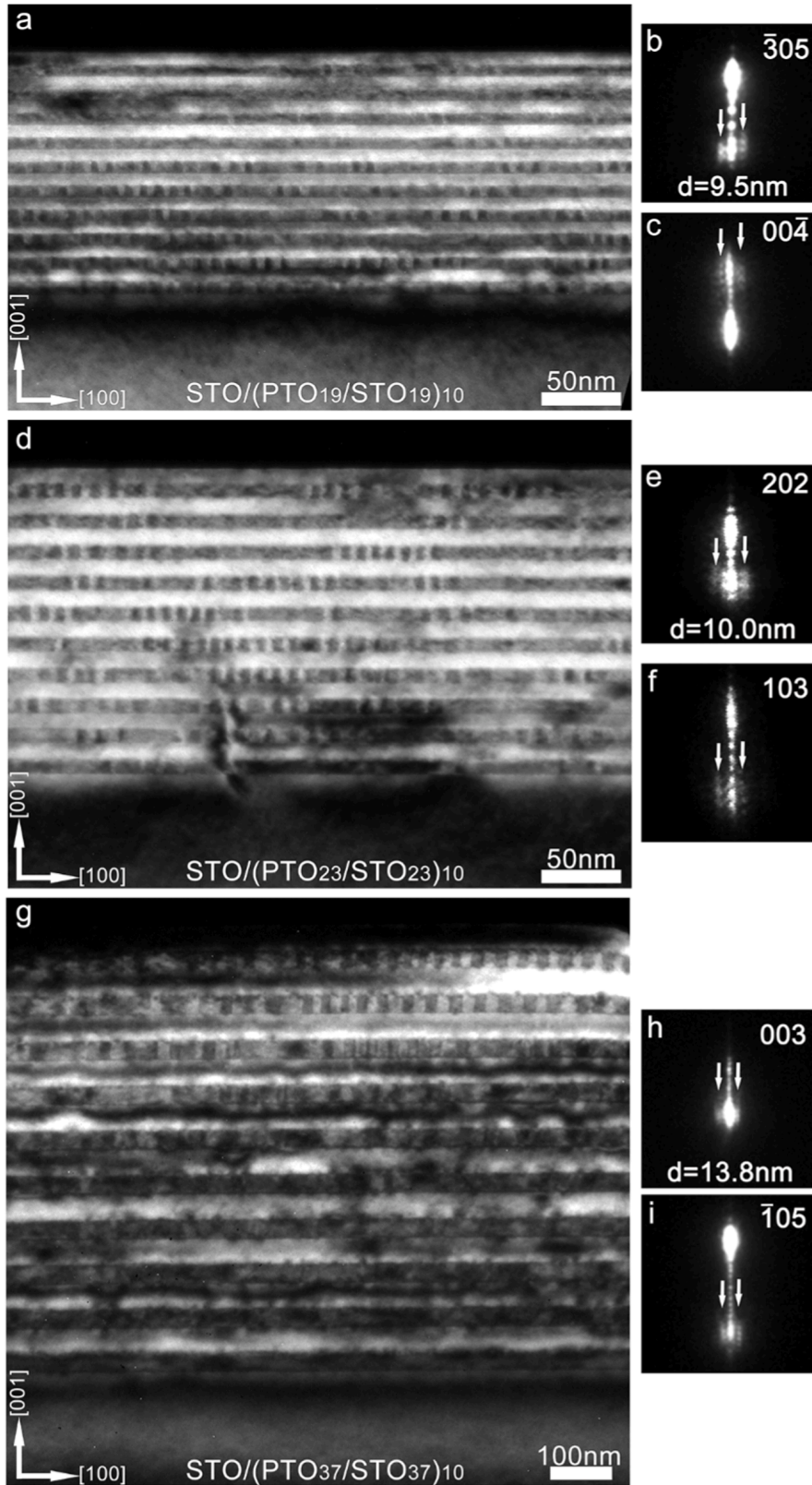


Fig. 1. Diffraction contrast analysis. (a-i) Cross-sectional dark field TEM images of $[(\text{PTO})_m/(\text{STO})_m]_{10}$ ($m = 19, 23, 37$ u.c.) superlattices grown on STO (001) substrate, along with the corresponding single SAED spots of these $[(\text{PTO})_m/(\text{STO})_m]_{10}$ ($m = 19, 23, 37$ u.c.) superlattices. The single SAED spots ($\bar{3}05$, $00\bar{4}$, 202 , 103 , 003 , $\bar{1}05$) from the area including the substrate and superlattices.

$$\frac{\partial P_i(x, t)}{\partial t} = -L \frac{\delta F}{\delta P_i(x, t)}, (i = 1, 2, 3) \quad (9)$$

where t is the time step, L is the kinetic coefficient related to the domain wall mobility. We use the backward Euler method to trace the evolution of polarization.

3. Results and discussions

In this work, we grew a series of $[(\text{PTO})_m/(\text{STO})_m]_n$ ($m = 12, 19, 23, 27, 37$ u.c., $n = 10$) superlattices with varying thickness on STO substrates. The $[001]$ orientation indicates the out-of-plane direction, which is the direction of film growth. Fig. 1(a-i) shows the cross-sectional dark field TEM images of $[(\text{PTO})_m/(\text{STO})_m]_n$ ($m = 19, 23, 37$ u.c., $n = 10$) superlattices, along with the corresponding selected area electron diffraction (SAED) patterns. From Fig. 1(a,d,g), it can be seen that the interfaces of STO/PTO are flat. Some strip-like areas showing bright and dark contrast are observed in the PTO layers of the superlattices. These contrasts are approximately perpendicular to the STO/PTO interfaces and exhibit locally ordered characteristics. As the thickness of the $[(\text{PTO})_m/(\text{STO})_m]_n$ superlattices increases from 19 u.c. to 23 u.c., and finally to 37 u.c., the morphologies of the superlattices are shown in Fig. 1(a,d,g). It should be noted that with increasing the superlattice thickness, the periods of the stripe-like areas also increase accordingly. Additionally, in the planar view, the 180° domains also exhibit strip characteristics, while skyrmion-bubble domains appear with circular or elongated features. In the cross-sectional view, there is no significant difference in the diffraction contrast images between the 180° domains and skyrmion-bubble domains. Thus, based solely on the morphological features observed in the cross-sectional view, it is easy to assume that these stripe-like domains are 180° domains. However, previous result has proven that these are actually skyrmion-bubble domains.

To accurately determine the periods of skyrmion-bubbles, SAED experiments are performed on cross-sectional TEM samples. TEM is a

powerful tool for determining the crystal structure and periodic information. Fig. 1(b,c,e,f,h,i) show single enlarged $\bar{3}05$, 004 , 202 , 103 , 003 and $\bar{1}05$ SAED spots, respectively. These single high-index diffraction spots are complex. The middle row of diffraction spots represents Bragg diffraction spot. The superlattice Bragg reflections indicate the long-range ordering along the out-of-plane direction. Particularly, satellite diffraction spots marked by a pair of white arrows indicate out-of-plane ordering layer by layer and in-plane local ordering modulations of skyrmion-bubbles. The ordering satellite diffraction spots originate from skyrmion-bubble and are consistent with the DF images. The distance between the Bragg diffraction spots reflects the total thickness of the superlattice and the thickness of one PTO/STO period. The in-plane modulation period (d) of skyrmion-bubbles can be calculated via the distance between the satellite peak and the Bragg peak

$$d = \frac{1}{\Delta q_x}, \quad (10)$$

which yields in-plane periods of 9.5, 10.0, 13.8 nm, respectively.

To elucidate the microstructure of the skyrmion-bubble, we performed the planar view dark field STEM imaging and atomic scale polarization mapping using a displacement vector algorithm on cross-sectional high angle annular dark field (HAADF) STEM images, alongside lattice rotation angle analysis (Fig. 2). Fig. 2(a) shows the planar view under-focus dark field STEM image of $(\text{PTO}_{27}/\text{STO}_{27})_{10}$ superlattices, revealing the widespread presence of nanometre size round and elongated characteristics. In the cross-sectional HAADF-STEM image, the positions of Pb and Ti atom columns are marked by solid yellow and red circles, respectively (Fig. 2(b)). The Pb^{2+} atom columns appear as the brightest dots, while the Ti^{4+} atom columns exhibit weaker contrast. This difference in contrast arises because, in the HAADF-STEM imaging, the intensity of an atom column is approximately proportional to Z^2 , where Z is the atomic number. We then extracted the polarization map of the skyrmion-bubble (Fig. 2(c)), which shows a polarization direction opposite to the displacement direction of Ti^{4+} . The polarization map distinctly reveals a cylindrical polar region with anti-parallel

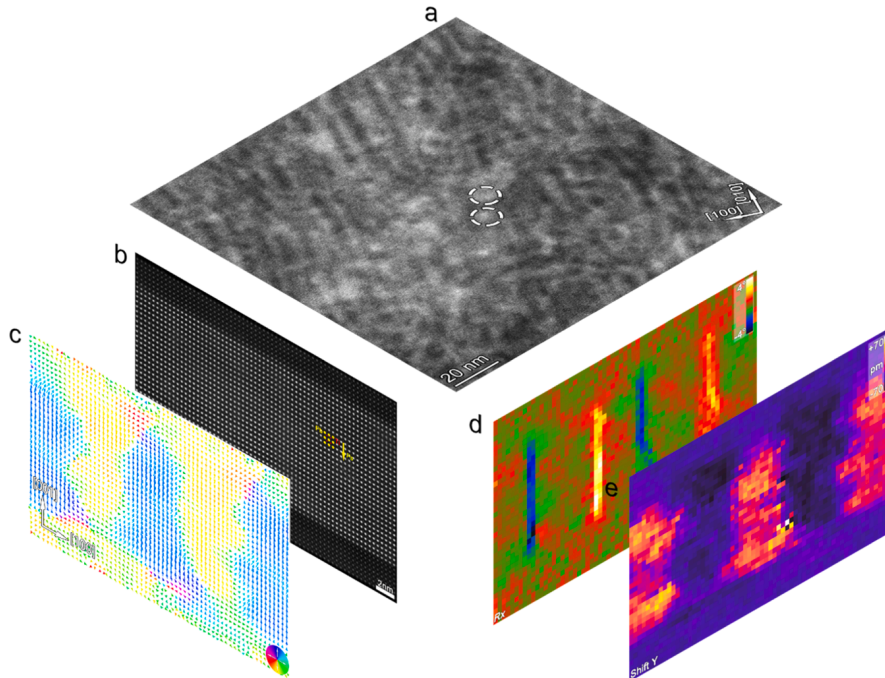


Fig. 2. Ferroelectric skyrmion-bubbles characterization. (a) Planar view dark field under-focus STEM imaging of $(\text{PTO}_{27}/\text{STO}_{27})_{10}$ superlattices, showing a widespread distribution of both rounded and elongated skyrmion-bubbles. A single skyrmion-bubble is highlighted with a white dotted circle. (b) Cross-sectional HAADF-STEM images of $(\text{PTO}_{27}/\text{STO}_{27})_{10}$ superlattices. The Pb and Ti atom columns are marked by yellow and red circles, respectively, while the yellow arrow indicates the spontaneous polarization (P_s) direction, which corresponds to the reversed Ti-displacement vectors (δ_{Ti}). (c) The P_s maps illustrating the microstructure characteristics of the skyrmion-bubbles. (d) The 2D mapping of the lattice rotation (R_x). (e) The displacement of Ti along the out-of-plane direction (shift Y).

polarization. Furthermore, the polarization vector undergoes rotation at the boundaries near the PTO/STO interfaces, aligning with the divergence characteristics typical of skyrmion-bubbles. Fig. 2(d) shows the in-plane lattice rotation map (R_x), where counterclockwise rotation is defined as positive. In the domain wall region of the skyrmion-bubble, the lattice rotation angle is approximately 3° . The lattice rotation angle gradually decreases as it crosses the domain wall of the skyrmion-bubble. Fig. 2(e) shows the out-of-plane displacement of Ti^{4+} . The out-of-plane displacement of Ti^{4+} is 70 pm to -70 pm from the left side of the domain wall to the right. The position with the minimal ion displacement in Fig. 2(e) is usually near the domain wall, as the Bloch-type regions of the skyrmion-bubble mainly exhibit in-plane displacement components.

The microstructure and the out-of-plane lattice strain (ϵ_{yy}) of the 180° stripe domains in PTO films on STO substrate, as well as the skyrmion-bubbles in STO/PTO/STO films on STO substrate, were analyzed using phase field simulations. Fig. 3(a) and 3(b) show the planar view and the cross section of the 180° stripe domain, indicating that there is no in-plane polarization on the surface of the PTO film. As shown in Fig. 3(c), the out-of-plane strain distribution is uniform. Fig. 3(d) illustrates the planar view of the skyrmion-bubbles domain structure on the upper surface of the PTO layer. The black arrows indicate the in-plane polarization vectors, highlighting the polarization divergence characteristics of the skyrmion-bubbles on the upper surface. In Fig. 3(e), the cross-sectional view reveals continuous rotation: on the upper surface, the upward polarization continuously rotates downward, while on the lower surface, the downward polarization continuously rotates gradually upward. Finally, Fig. 3(f) depicts the out-of-plane strain distributions in the skyrmion-bubble structures. The main part of the skyrmion-bubble exhibits a uniform out-of-plane strain, with a smaller out-of-plane strain present at the domain walls, where in-plane polarization is observed.

According to previous research, flux-closure exhibits significant

disclination strain, with strain gradients reaching up to 10^9 per meter [1]. Additionally, periodic strain fluctuations are also observed in vortex arrays, likely due to the potential correlation among flux-closures, vortices, and trivial ferroelastic domains (a/c , a_1/a_2) [36–39]. However, the skyrmion-bubbles differ considerably from flux-closures and vortices, and whether they are subject to strain modulation remains unclear. Next, to clarify the possible origin of the skyrmion-bubbles, we obtained the strain distribution maps based on the geometric phase analysis (GPA) for both 180° domain and skyrmion-bubbles. Fig. 4(a–d) presents the low-magnification HAADF-STEM image of 180° domain in BiFeO_3 (BFO) film and the corresponding maps of in-plane strain (ϵ_{xx}), out-of-plane strain (ϵ_{yy}), and in-plane lattice rotation angle (R_x). For 180° domain structures, the single BFO layer was grown on a PrScO_3 substrate. In Fig. 4(a), we observe alternating regions of enhanced white contrast in the BFO layer, which may correspond to the variations in strain and lattice rotation angle shown in Fig. 4(b–d). Fig. 4(e–h) presents the low-magnification HAADF-STEM image of skyrmion-bubbles, along with the corresponding maps of ϵ_{xx} , ϵ_{yy} , and R_x . For skyrmion-bubbles structures, the PTO/STO superlattice was grown on a STO substrate. In the PTO/STO superlattice, the PTO layer exhibits a slight in-plane strain and a pronounced, uniform out-of-plane tensile strain, with no significant strain fluctuations, suggesting that the appearance of skyrmion-bubble is not strongly correlated with in-plane strain (Fig. 4(f, g)). The presence of skyrmion-bubbles can be traced through the in-plane lattice rotation maps, which also indicate that their distribution of skyrmion-bubbles exhibits locally ordered characteristics (Fig. 4(h)). To some extent, GPA analysis further confirms that the strain distribution of skyrmion-bubbles is similar to that of 180° domain, suggesting that the appearance of skyrmion-bubbles may originate from 180° domain. When the PTO layer is clamped by symmetric insulating STO layers, the depolarization field acts like a blade, slicing the stripe-shaped 180° domains into circular or elongated skyrmion-bubbles. For the $[(\text{PTO})_m/(\text{STO})_n]_n$ ($m = 12, 23$ u.c., $n = 10$) superlattices (Fig. 4(e–l)),

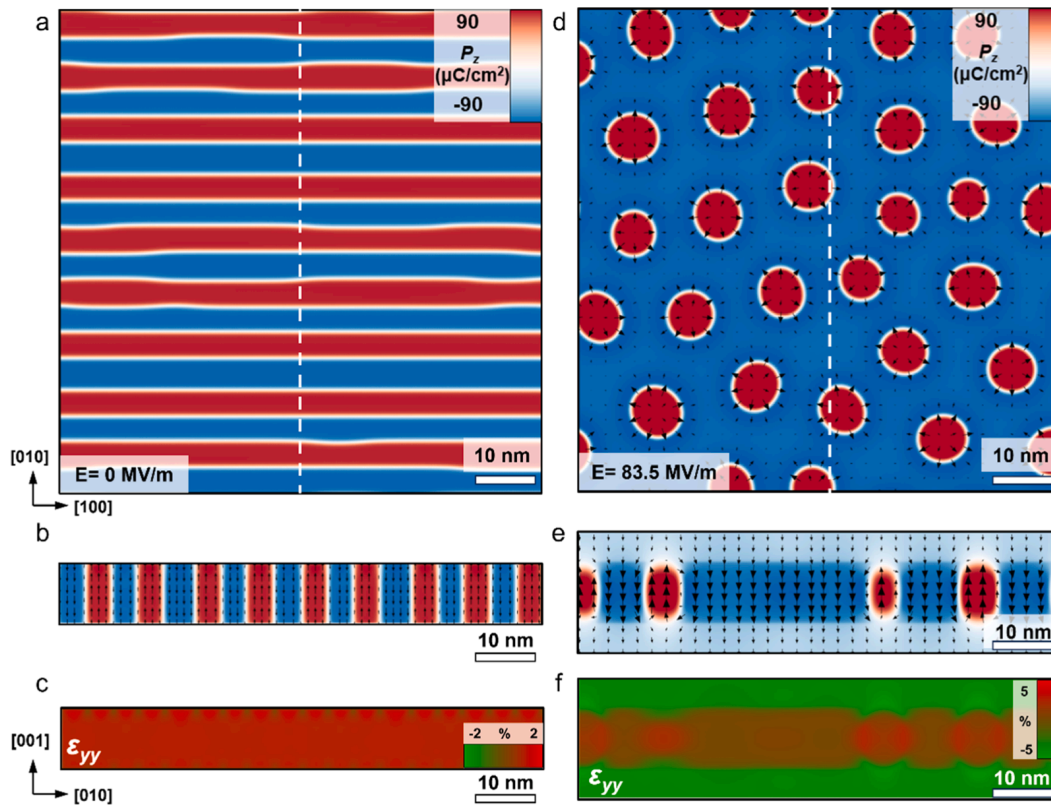


Fig. 3. Ferroelectric 180° stripe domain and the skyrmion-bubbles obtained by phase field simulation. (a–c) The planar view, the cross-sectional, and the out-of-plane lattice strain ϵ_{yy} of the 180° stripe domain in the PTO film, respectively. (d–f) The planar view, the cross-sectional, and the out-of-plane lattice strain ϵ_{yy} of skyrmion-bubbles in the STO/PTO/STO film with the electric field of 83.5 MV/m, respectively.

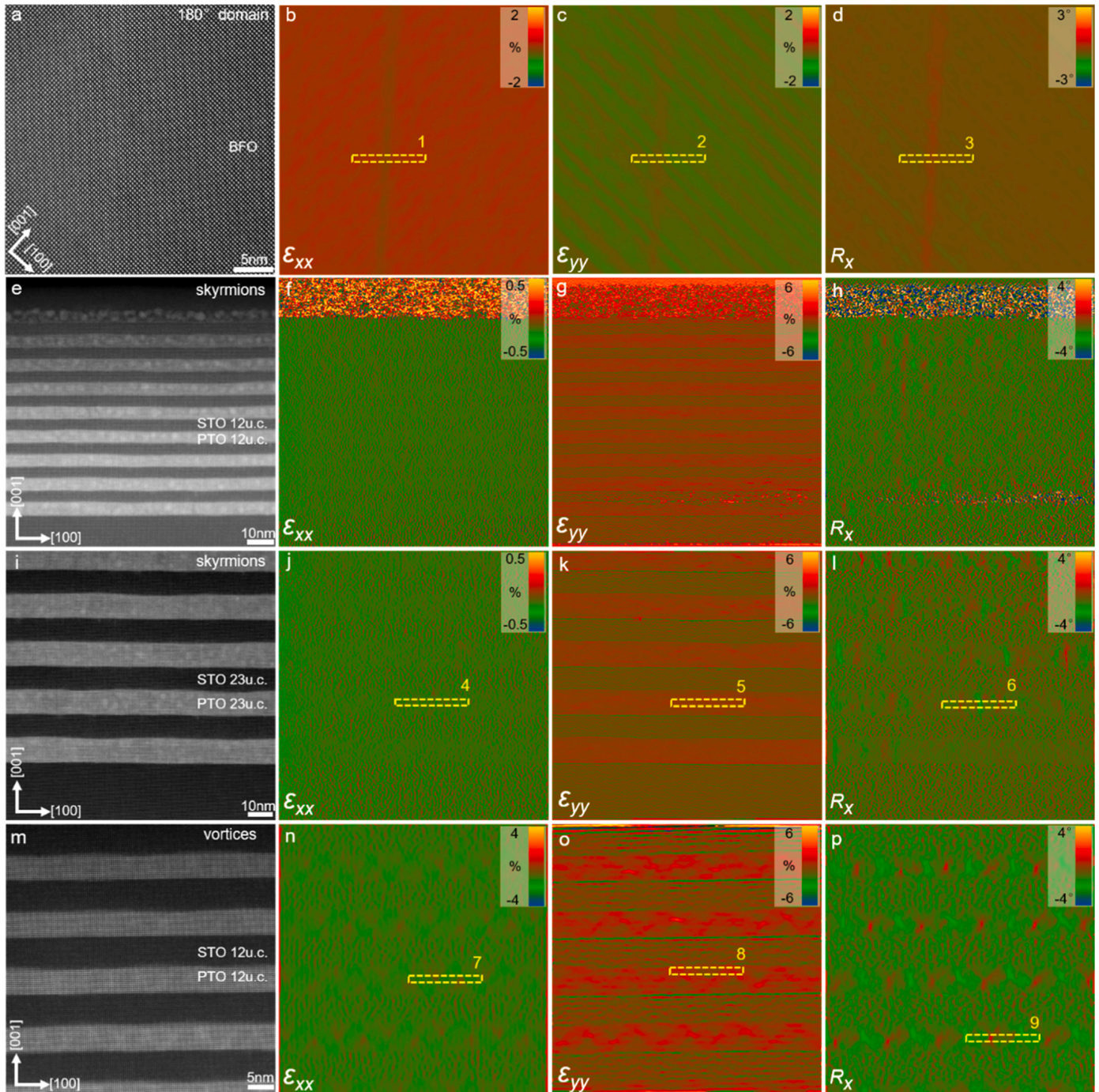


Fig. 4. Comparative GPA analysis of 180° domain, skyrmion-bubbles and vortices. (a-d) The low-magnification HAADF-STEM image of the 180° domain alongside corresponding in-plane lattice strain (ϵ_{xx}), out-of-plane lattice strain (ϵ_{yy}) and in-plane lattice rotation (R_x). (e-h, i-l) The low-magnification HAADF-STEM images of skyrmion-bubble structures in PTO/STO superlattices of varying thicknesses, with corresponding maps of ϵ_{xx} , ϵ_{yy} and R_x . (m-p) The low-magnification HAADF-STEM images of the vortices alongside corresponding ϵ_{xx} , ϵ_{yy} and R_x . Line profiles for regions 1 ~ 9 are presented in Fig. 5.

the GPA analysis results are consistent, indicating that the superlattice thickness has minimal effect on the formation of skyrmion-bubbles and confirming that skyrmion-bubbles may originate from 180° domain. In addition, we have also grown the PTO/STO superlattice on the DyScO₃ substrate and completed the strain analysis of the periodic vortex arrays (Fig. 4(m-p)). Fig. 4(m-p) present the low-magnification HAADF-STEM image of vortices and the corresponding maps of ϵ_{xx} , ϵ_{yy} , and R_x . In Fig. 4(m), we observe periodically alternating regions of enhanced white contrast in the PTO layer, which may correspond to the variations in lattice rotation angles shown in Fig. 4(p). The red-colored sinusoidal wave pattern along the [100] direction suggests the long range ordering of clockwise and anticlockwise vortex structures, whereas no such

feature is seen in STO layers (Fig. 4(o)). The strain map of vortices shows significant strain fluctuations, exhibiting characteristics of ferroelastic domains, and is highly likely to originate from ferroelastic domains.

Fig. 5 shows the line profiles of 180° domain, skyrmion-bubbles, and vortices labeled 1 to 9 in Fig. 4. Fig. 5(a-c) are the line profiles (ϵ_{xx} , ϵ_{yy} , R_x) of 180° domain. It should be additionally noted that the inclined 45° stripes are caused by scanning noise. The ϵ_{xx} strain line profile shows that the domain wall positions experience significant compressive strain along the in-plane direction. The black arrows indicate the 180° domain walls have a certain width, approximately spanning a few unit cells, as shown in Fig. 5(a). The ϵ_{yy} strain line profile shows the domain wall positions experience significant tensile strain along the out-of-plane

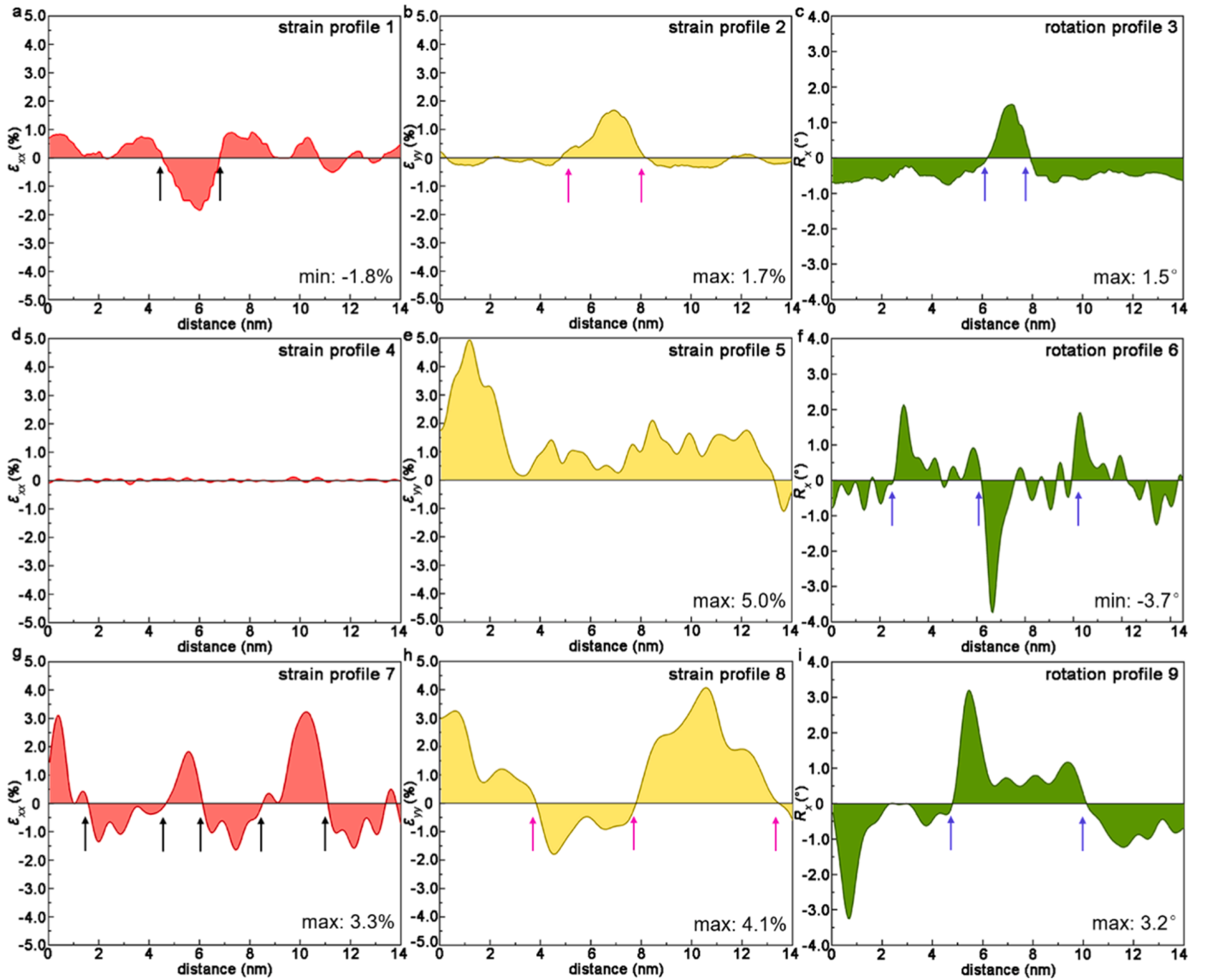


Fig. 5. Comparative line profile GPA analysis of 180° domain, skyrmion-bubbles, and vortices. (a-c) The line profiles of 180° domain for the ϵ_{xx} , ϵ_{yy} , and R_x . (d-f) The line profiles of skyrmion-bubbles for the ϵ_{xx} , ϵ_{yy} , and R_x . (g-i) The line profiles of vortices for the ϵ_{xx} , ϵ_{yy} , and R_x . The arrows denote the rotation areas of P_s .

direction. Similarly, the pink arrows also indicate the positions where tensile strain transitions to compressive strain (Fig. 5(b)). The R_x line profile shows local maximum of about 1.5° . The blue arrows indicate the positions where the lattice transitions from clockwise rotation to counterclockwise rotation and from counterclockwise rotation to clockwise rotation (Fig. 5(c)). It is noted that the strain and lattice rotations are very inhomogeneous distribution. However, for skyrmion-bubble, the ϵ_{xx} is nearly zero because the in-plane lattice constants of STO ($a = 3.905 \text{ \AA}$) and PTO ($a = 3.899 \text{ \AA}$) are very similar (Fig. 5(d)). The PTO/STO superlattice exhibits out-of-plane strain modulations (Fig. 5(e)). The in-plane and out-of-plane strain distributions of the skyrmion-bubble do not show any alternating fluctuations of tension or compression. The R_x variation of the skyrmion-bubble is relatively significant. The blue arrow indicates the position where the lattice rotation gradually transitions, as shown in Fig. 5(f). Fig. 5(g-i) are the line profiles (ϵ_{xx} , ϵ_{yy} , R_x) of vortices. The ϵ_{xx} strain line profile shows local maximum of about 3.3% around the vertices of the vortices. The black arrows indicate the positions where tensile strain transitions to compressive strain (Fig. 5(g)). The ϵ_{xx} line profile shows local maximum of about 3.3%, which is quite larger than the cases of 180° domains (-1.8%) and skyrmion-bubbles (0%). In addition, it is noted that the inhomogeneous distribution of the ϵ_{yy} appears in Fig. 5(h). The blue arrows indicate the positions where the

lattice transitions from clockwise rotation to counterclockwise rotation (Fig. 5(i)). Therefore, the ϵ_{xx} lattice strain of vortices is larger than that of 180° domains and skyrmion-bubbles.

If we directly grow single PTO film on the STO substrate, 180° domains will form in the PTO layer (Fig. 6(a)). If we directly grow PTO/STO superlattices on the STO substrate, skyrmion-bubbles will form in the PTO layer (Fig. 6(b)). When we grow single PTO film on DyScO₃ (DSO) and NdScO₃ (NSO) substrates, a/c and a_1/a_2 domains will form in the PTO layers, respectively (Fig. 6(c)). If the normal direction of the domain wall is perpendicular to the observation direction (electron beam direction), the domain wall appears sharp. However, if the normal direction of the domain wall is not perpendicular to the observation direction, the domain wall appears blurred. For example, in the cross-sectional view, the observation direction [100] is perpendicular to the normal direction of the a/c domain wall, so the a/c domain wall appears sharp. In contrast, in the planar view, the observation direction [001] is not perpendicular to the normal direction of the a/c domain wall, causing the domain wall to appear blurred. If we grow PTO/STO superlattice on DSO and NSO substrates, flux-closure or vortex structures will form in the PTO layer (Fig. 6(d)). The vortex and flux-closure are highly prone to transform into a/c and a_1/a_2 domains. In the cross-sectional view, the morphological characteristics of skyrmion-bubbles

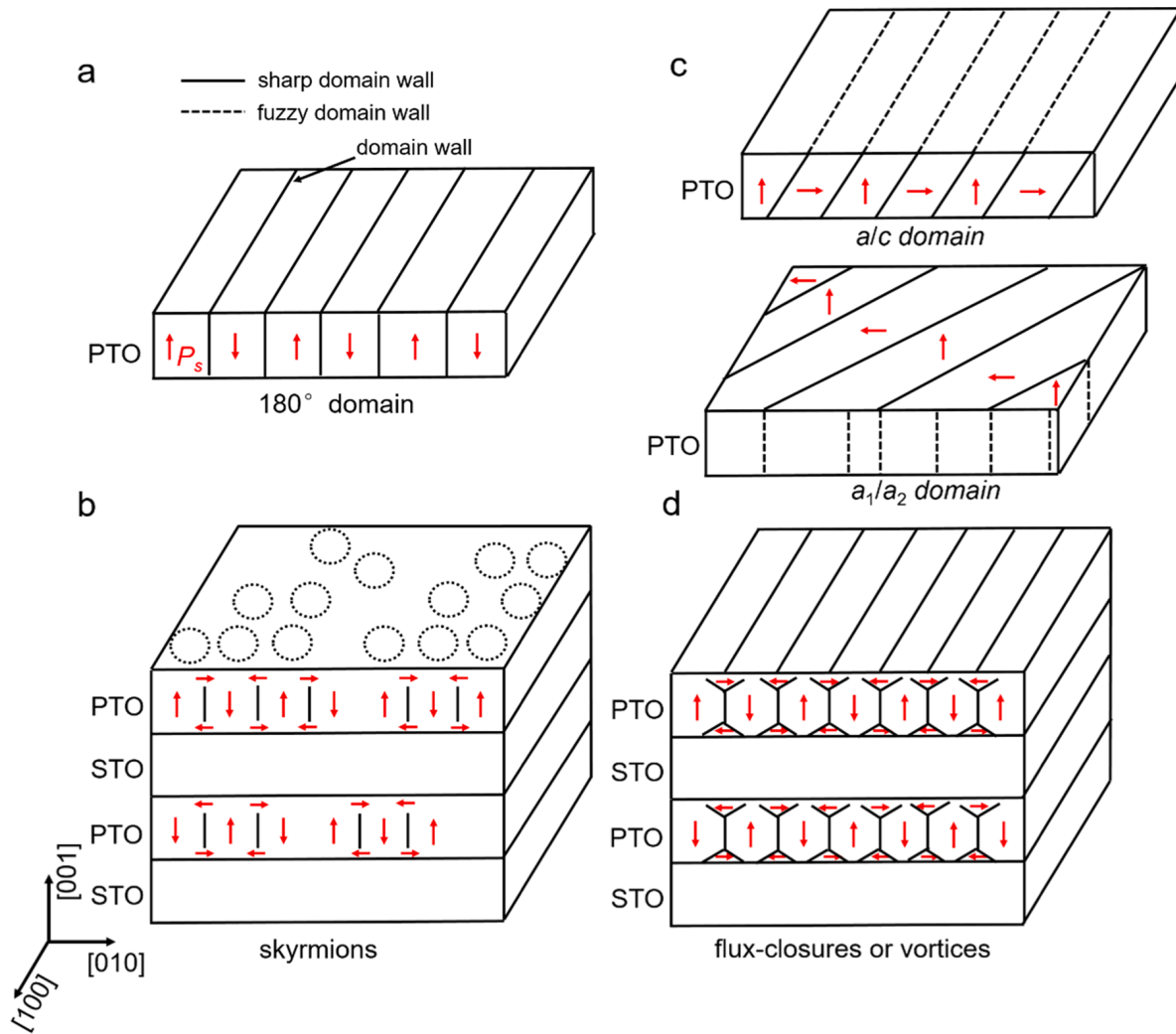


Fig. 6. Trivial and nontrivial domains. (a,b) 3D schematic diagrams of ferroelectric 180° domains and ferroelectric skymion-bubbles. (c,d) 3D schematic diagrams of ferroelastic a/c , a_1/a_2 domains and ferroelastic flux-closures, vortices.

and 180° domain appear similar, while in the planar view, skymions exhibit distinct circular or elongated features. These observations are crucial for identifying the structure of skymions through planar morphology analysis (Fig. 6). The formation mechanism of skymion-bubble is fundamentally different from that of vortices and flux-closures. GPA and phase field simulation indicate that skymion-bubble may originate from ferroelectric domains (180° domains), whereas vortices and flux-closure structures are likely associated with ferroelastic domains (a/c , a_1/a_2). Furthermore, to validate the universality of our conclusion, we performed additional phase-field simulations of domain evolution in LiNbO_3 thin films. The results demonstrate that even in non-ferroelastic systems, ferroelectric 180° stripe domains can transform into skymion-bubble configurations under applied out-of-plane electric fields when open-circuit boundary conditions are maintained (Supplementary Materials).

4. Conclusion

In this study, we have grown a series of PTO/STO superlattices with varying thicknesses and utilized various experimental techniques, including diffraction contrast analysis, SAED, polarization analysis, and GPA, to investigate the morphological characteristics, periodicity, and strain information of skymion-bubbles, in an attempt to clarify the formation mechanisms of skymion-bubbles. The result are as follows:

- (1) Diffraction contrast analysis and SAED together confirm the period of the skymion-bubbles for the $[(\text{PTO})_n/(\text{STO})_n]_{10}$ ($n = 19, 23, 37$ u.c.) superlattice grown on the STO substrate is 9.5, 10.0, 13.8 nm, respectively. Skymion-bubbles exhibit localized ordered distributions characteristics.
- (2) In the PTO layer of the PTO/STO superlattice grown on the STO substrate, there is a uniform, slight compressive strain in the in-plane direction and a uniform tensile strain modulation in the out-of-plane direction. This suggests that strain does not play a key role in the formation of skymion-bubbles. In contrast, the vortex structures formed in the PTO layer of the PTO/STO superlattice experience periodic strain modulation both in-plane and out-of-plane, suggesting that the formation of vortices is dependent on strain. Based on these experimental results, skymion-bubbles are formed through the evolution of 180° domains under the influence of the depolarization field. This indicates a genetic relationship between skymion-bubbles and 180° domains.

Author declarations

Author contributions

X.L.M. conceived the idea of the work. Y.L.T. and Y.L.Z. guided the projects. F.H.G., Y.T.C. and M.J.H. fabricated the films and performed the TEM/STEM experiments. H.M.L., K.M.L. and Y.J.W. conducted the

phase field simulation. F.H.G. and Y.T.C. wrote the manuscript with contributions from others. All authors contributed to the discussions and manuscript preparation.

Data availability

The data that support the findings of this study are available from the corresponding authors upon reasonable request.

CRediT authorship contribution statement

Feng-Hui Gong: Writing – review & editing, Visualization, Investigation, Formal analysis, Conceptualization, Writing – original draft, Methodology, Funding acquisition, Data curation. **Yu-Ting Chen:** Writing – original draft, Methodology, Funding acquisition, Data curation, Writing – review & editing, Visualization, Investigation, Formal analysis, Conceptualization. **Hui-Mei Li:** Validation, Formal analysis, Writing – review & editing, Software. **Kang-Ming Luo:** Data curation, Formal analysis, Investigation, Writing – original draft. **Meng-Jiao Han:** Writing – review & editing, Data curation, Formal analysis. **Yu-Jia Wang:** Visualization, Funding acquisition, Writing – review & editing, Software, Formal analysis. **Yun-Long Tang:** Writing – review & editing, Project administration, Conceptualization, Supervision, Formal analysis. **Yin-Lian Zhu:** Writing – review & editing, Project administration, Formal analysis, Supervision, Funding acquisition, Conceptualization. **Xiu-Liang Ma:** Writing – review & editing, Funding acquisition, Supervision, Conceptualization.

Declaration of competing interest

The authors declare that they have no known competing financial interests or personal relationships that could have appeared to influence the work reported in this paper.

Acknowledgements

This work is supported by the National Natural Science Foundation of China (no. 52122101, 51971223), Guangdong Provincial Quantum Science Strategic Initiative (no. GDZX2202001, GDZX2302001) and Shenyang National Laboratory for Materials Science (L2022R04, L2021F06). F.H.G. acknowledges the China National Postdoctoral Program for Innovative Talents (no. BX20240245) and the China Postdoctoral Science Foundation (no. 2024M752303), Y.T.C. acknowledges the China Postdoctoral Science Foundation (no. 2023M742519), Y.J.W. acknowledges the Youth Innovation Promotion Association CAS (no. 2021187).

Supplementary materials

Supplementary material associated with this article can be found, in the online version, at [doi:10.1016/j.actamat.2025.121481](https://doi.org/10.1016/j.actamat.2025.121481).

References

- Y.L. Tang, Y.L. Zhu, X.L. Ma, A.Y. Borisevich, A.N. Morozovska, E.A. Eliseev, W. Y. Wang, Y.J. Wang, Y.B. Xu, Z.D. Zhang, S.J. Pennycook, Observation of a periodic array of flux-closure quadrants in strained ferroelectric PbTiO₃ films, *Science* 348 (2015) 547–551.
- X.M. Li, C.B. Tan, C. Liu, P. Gao, Y.W. Sun, P. Chen, M.Q. Li, L. Liao, R.X. Zhu, J. B. Wang, Y.C. Zhao, L.F. Wang, Z. Xu, K.H. Liu, X.L. Zhong, J. Wang, X.D. Bai, Atomic-scale observations of electrical and mechanical manipulation of topological polar flux closure, *Proc. Natl. Acad. Sci.* 117 (2020) 18954–18961.
- C.T. Nelson, B. Winchester, Y. Zhang, S.J. Kim, A. Melville, C. Adamo, C. M. Folkman, S.H. Baek, C.B. Eom, D.G. Schlom, L.Q. Chen, X.Q. Pan, Spontaneous vortex nanodomain arrays at ferroelectric heterointerfaces, *Nano. Lett.* 11 (2011) 828–834.
- A.K. Yadav, C.T. Nelson, S.L. Hsu, Z.J. Hong, J.D. Clarkson, C.M. Schlepütz, A. R. Damodaran, P. Shafer, E. Arenholz, L.R. Dedon, D. Chen, A. Vishwanath, A. M. Minor, L.Q. Chen, J.F. Scott, L.W. Martin, R. Ramesh, Observation of polar vortices in oxide superlattices, *Nature* 530 (2016) 198–201.
- G. Sánchez-Santolino, V. Rouco, S. Puebla, H. Aramberri, V. Zamora, M. Cabero, F. A. Cuellar, C. Munuera, F. Mompean, M. Garcia-Hernandez, A. Castellanos-Gomez, J. Íñiguez, C. Leon, J. Santamaria, A 2D ferroelectric vortex pattern in twisted BaTiO₃ freestanding layers, *Nature* 626 (2024) 529–534.
- Y.J. Wang, Y.P. Feng, Y.L. Zhu, Y.L. Tang, L.X. Yang, M.J. Zou, W.R. Geng, M. J. Han, X.W. Guo, X.L. Ma, B.Wu, Polar meron lattice in strained oxide ferroelectrics, *Nat. Mater.* 19 (2020) 881–886.
- F.H. Gong, Y.L. Tang, Y.L. Zhu, H. Zhang, Y.J. Wang, Y.T. Chen, Y.P. Feng, M. J. Zou, B. Wu, W.R. Geng, Y. Cao, X.L. Ma, Atomic mapping of periodic dipole waves in ferroelectric oxide, *Sci. Adv.* 7 (2021) eabg5503.
- Q. Li, V.A. Stoica, M. Paściak, Y. Zhu, Y.K. Yuan, T.N. Yang, M.R. McCarter, S. Das, A.K. Yadav, S. Park, C. Dai, H.J. Lee, Y. Ahn, S.D. Marks, S.K. Yu, C. Kadlec, T. Sato, M.C. Hoffmann, M. Chollet, M.E. Kozina, S. Nelson, D.L. Zhu, D.A. Walko, A. M. Lindenberg, P.G. Evans, L.Q. Chen, R. Ramesh, L.W. Martin, V. Gopalan, J. W. Freeland, J. Hlinka, H.D. Wen, Subterahertz collective dynamics of polar vortices, *Nature* 592 (2021) 376–380.
- D. Rusu, J.J.P. Peters, T.P.A. Hase, J.A. Gott, G.A.A. Nisbet, J. Stremper, D. Haskel, S.D. Seddon, R. Beanland, A.M. Sanchez, M. Alexe, Ferroelectric incommensurate spin crystals, *Nature* 602 (2022) 240–244.
- J. Ma, J. Ma, Q.H. Zhang, R.C. Peng, J. Wang, C. Liu, M. Wang, N. Li, M.F. Chen, X. X. Cheng, P. Gao, L. Gu, L.Q. Chen, P. Yu, J.X. Zhang, C.W. Nan, Controllable conductive readout in self-assembled, topologically confined ferroelectric domain walls, *Nat. Nanotech.* 13 (2018) 947–952.
- Y. Nahas, S. Prokhorenko, J. Fischer, B. Xu, C. Carrétero, S. Prosandeev, M. Bibes, S. Fusil, B. Dkhil, V. Garcia, L. Bellaiche, Inverse transition of labyrinthine domain patterns in ferroelectric thin films, *Nature* 577 (2020) 47–50.
- Z.W. Li, Y.J. Wang, G. Tian, P.L. Li, L.N. Zhao, F.Y. Zhang, J.X. Yao, H. Fan, X. Song, D.Y. Chen, Z. Fan, M.H. Qin, M. Zeng, Z. Zhang, X.B. Lu, S.J. Hu, C.H. Lei, Q.F. Zhu, J.Y. Li, X.S. Gao, J.M. Liu, High-density array of ferroelectric nanodots with robust and reversibly switchable topological domain states, *Sci. Adv.* 3 (2017) e1700919.
- M. Hadjimichael, Y.Q. Li, E. Zatterin, G.A. Chahine, M. Conroy, K. Moore, E.N. O'Connell, P. Ondrejčević, P. Marton, J. Hlinka, U. Bangert, S. Leake, P. Zubko, Metal–ferroelectric supercrystals with periodically curved metallic layers, *Nat. Mater.* 20 (2021) 495–502.
- S. Das, Y.L. Tang, Z.J. Hong, M.A.P. Gonçalves, M.R. McCarter, C. Klewe, K. X. Nguyen, F. Gómez-Ortiz, P. Shafer, E. Arenholz, V.A. Stoica, S.L. Hsu, B. Wang, C. Ophus, J.F. Liu, C.T. Nelson, S. Saremi, B. Prasad, A.B. Mei, D.G. Schlom, J. Íñiguez, P. García-Fernández, D.A. Müller, L.Q. Chen, J. Junquera, L.W. Martin, R. Ramesh, Observation of room-temperature polar skyrmions, *Nature* 568 (2019) 368–372.
- F.H. Gong, Y.L. Tang, Y.J. Wang, Y.T. Chen, B. Wu, L.X. Yang, Y.L. Zhu, X.L. Ma, Absence of critical thickness for polar skyrmions with breaking the Kittel's law, *Nat. Commun.* 14 (2023) 3376.
- L. Han, C. Addiego, S. Prokhorenko, M.Y. Wang, H.Y. Fu, Y. Nahas, X.X. Yan, S. H. Cai, T.Q. Wei, Y.H. Fang, H.Z. Liu, D.X. Ji, W. Guo, Z.B. Gu, Y.R. Yang, P. Wang, L. Bellaiche, Y.F. Chen, D. Wu, Y.F. Nie, X.Q. Pan, High-density switchable skyrmion-like polar nanodomains integrated on silicon, *Nature* 603 (2022) 63–67.
- S. Das, Z.J. Hong, V.A. Stoica, M.A.P. Gonçalves, Y.T. Shao, E. Parsonnet, E. J. Marksz, S. Saremi, M.R. McCarter, A. Reynoso, C.J. Long, A.M. Hagerstrom, D. Meyers, V. Ravi, B. Prasad, H. Zhou, Z. Zhang, H. Wen, F. Gómez-Ortiz, P. García-Fernández, J. Bokor, J. Íñiguez, J.W. Freeland, N.D. Orloff, J. Junquera, L.Q. Chen, S. Salahuddin, D.A. Müller, L.W. Martin, R. Ramesh, Local negative permittivity and topological phase transition in polar skyrmions, *Nat. Mater.* 20 (2021) 194–201.
- S.X. Wang, W. Li, C.G. Deng, Z.J. Hong, H.B. Gao, X.L. Li, Y.L. Gu, Q. Zheng, Y. J. Wu, P.G. Evans, J.F. Li, C.W. Nan, Q. Li, Giant electric field-induced second harmonic generation in polar skyrmions, *Nat. Commun.* 15 (2024) 1374.
- A.I. Khan, A. Keshavarzi, S. Datta, The future of ferroelectric field-effect transistor technology, *Nat. Electron.* 3 (2020) 588–597.
- P. Zubko, N. Stucki, C. Lichtensteiger, J.M. Triscone, X-ray diffraction studies of 180° ferroelectric domains in PbTiO₃/SrTiO₃ superlattice under an applied electric field, *Phys. Rev. Lett.* 104 (2010) 187601.
- L.M. Zhou, Y.H. Huang, S. Das, Y.L. Tang, C. Li, H. Tian, L.Q. Chen, Y.J. Wu, R. Ramesh, Z.J. Hong, Local manipulation and topological phase transitions of polar skyrmions, *Matter* 5 (2022) 1031–1041.
- R.X. Zhu, Z.X. Jiang, X.X. Zhang, X.L. Zhong, C.B. Tan, M.W. Liu, Y.W. Sun, X.M. Li, R.S. Qi, K. Qu, Z.T. Liu, M. Wu, M.Q. Li, B.Y. Huang, Z. Xu, J.B. Wang, K.H. Liu, P. Gao, J. Wang, J.Y. Li, X.D. Bai, Dynamics of polar skyrmion bubbles under electric fields, *Phys. Rev. Lett.* 129 (2022) 107601.
- Y.T. Shao, S. Das, Z.J. Hong, R.J. Xu, S. Chandrika, F. Gómez-Ortiz, P. García-Fernández, L.Q. Chen, H.Y. Hwang, J. Junquera, L.W. Martin, R. Ramesh, D. A. Müller, Emergent chirality in a polar meron to skyrmion phase transition, *Nat. Commun.* 14 (2023) 1355.
- S. Yuan, Z.H. Chen, S. Prokhorenko, Y. Nahas, L. Bellaiche, C.H. Liu, B. Xu, L. Cheng, S. Das, L.W. Martin, Hexagonal close-packed polar-skyrmion lattice in ultrathin ferroelectric PbTiO₃ films, *Phys. Rev. Lett.* 130 (2023) 226801.
- H.M. Li, Y.J. Wang, Y.L. Tang, Y.L. Zhu, X.L. Ma, Evolution of solitons in the PbTiO₃/SrTiO₃ multilayer film driven by the electric field, *Acta Mater* 289 (2025) 120882.
- L.Y. Gao, S. Prokhorenko, Y. Nahas, L. Bellaiche, Dynamical control of topology in polar skyrmions via twisted light, *Phys. Rev. Lett.* 132 (2024) 026902.

- [27] Y.T. Chen, Y.L. Tang, Y.L. Zhu, Y.J. Wang, M.J. Han, M.J. Zou, Y.P. Feng, W. R. Geng, F.H. Gong, X.L. Ma, Periodic vortex-antivortex pairs in tensile strained PbTiO_3 films, *Appl. Phys. Lett.* 117 (2020) 192901.
- [28] Y.T. Chen, Y.L. Tang, F.H. Gong, B. Wu, M.J. Han, M.J. Zou, Y.P. Feng, Y.J. Wang, Y.L. Zhu, X.L. Ma, Direct observation of large-scale screw dislocation grids in oxide, *Nano Lett.* 22 (2022) 2085–2093.
- [29] M.J. Hÿtch, E. Snoeck, R. Kilaas, Quantitative measurement of displacement and strain fields from HREM micrographs, *Ultramicroscopy* 74 (1998) 131–146.
- [30] Y.Y. Zhu, C. Ophus, J. Ciston, H.Y. Wang, Interface lattice displacement measurement to 1 pm by geometric phase analysis on aberration-corrected HAADF STEM images, *Acta Mater* 61 (2013) 5646–5663.
- [31] E. Snoeck, B. Warot, H. Ardhuin, A. Rocher, M.J. Casanove, R. Kilaas, M.J. Hÿtch, Quantitative analysis of strain field in thin films from HRTEM micrographs, *Thin Solid Films* 319 (1998) 157–162.
- [32] E. Guerrero, P. Galindo, A. Yanez, T. Ben, S.I. Molina, Error quantification in strain mapping methods, *Microsc. Microanal.* 13 (2007) 320–328.
- [33] Y.L. Li, S.Y. Hu, Z.K. Liu, L.Q. Chen, Effect of substrate constraint on the stability and evolution of ferroelectric domain structures in thin films, *Acta Mater* 50 (2002) 395–411.
- [34] Y.L. Li, S.Y. Hu, D. Tenne, A. Soukiassian, D.G. Schlom, X.X. Xi, K.J. Choi, C. B. Eom, A. Saxena, T. Lookman, Q.X. Jia, L.Q. Chen, Prediction of ferroelectricity in $\text{BaTiO}_3/\text{SrTiO}_3$ superlattices with domains, *Appl. Phys. Lett.* 91 (2007) 112914.
- [35] Y.J. Wang, J. Li, Y.L. Zhu, X.L. Ma, Phase-field modeling and electronic structural analysis of flexoelectric effect at 180° domain walls in ferroelectric PbTiO_3 , *J. Appl. Phys.* 122 (2017) 224101.
- [36] K.S. Lee, J.H. Choi, J.Y. Lee, S. Baik, Domain formation in epitaxial $\text{Pb}(\text{Zr,Ti})\text{O}_3$ thin films, *J. Appl. Phys.* 90 (2001) 4095–4102.
- [37] A.R. Damodaran, S. Pandya, J.C. Agar, Y. Cao, R.K. Vasudevan, R.J. Xu, S. Saremi, Q. Li, J. Kim, M.R. McCarter, L.R. Dedon, T. Angsten, N. Balke, S. Jesse, M. Asta, S. V. Kalinin, L.W. Martin, Three-state ferroelastic switching and large electromechanical responses in PbTiO_3 thin films, *Adv. Mater.* 29 (2017) 1702069.
- [38] F.H. Gong, Y.L. Tang, Y.J. Wang, Y.T. Chen, B. Wu, L.X. Yang, Y.L. Zhu, X.L. Ma, Absence of critical thickness for polar skyrmions with breaking the Kittel's law, *Nat. Commun.* 14 (2023) 3376 [Supplementary Information] Available online: https://static-content.springer.com/esm/art%3A10.1038%2Fs41467-023-39169-y/MediaObjects/41467_2023_39169_MOESM1_ESM.pdf.
- [39] X.Y. Lu, Z.H. Chen, Y. Cao, Y.L. Tang, R.J. Xu, S. Saremi, Z. Zhang, L. You, Y. Q. Dong, S. Das, H.B. Zhang, L.M. Zheng, H.P. Wu, W.M. Lv, G.Q. Xie, X.J. Liu, J. Y. Li, L. Chen, L.Q. Chen, W.W. Cao, L.W. Martin, Mechanical-force-induced non-local collective ferroelastic switching in epitaxial lead-titanate thin films, *Nat. Commun.* 10 (2019) 3951.